

Supervise Less, See More: Training-free Nuclear Instance Segmentation with Prototype-Guided Prompting

Wen Zhang^{1,2}, Qin Ren¹, Wenjing Liu¹, Haibin Ling¹, Chenyu You¹

Accurate nuclear instance segmentation is a pivotal task in computational pathology, supporting data-driven clinical insights and facilitating downstream translational applications. While large vision foundation models have shown promise for zero-shot biomedical segmentation, most existing approaches still depend on dense supervision and computationally expensive fine-tuning. Consequently, training-free methods present a compelling research direction, yet remain largely unexplored. In this work, we introduce **SPROUT**, a fully training- and annotation-free prompting framework for nuclear instance segmentation. SPROUT leverages histology-informed priors to construct slide-specific reference prototypes that mitigate domain gaps. These prototypes progressively guide feature alignment through a partial optimal transport scheme. The resulting foreground and background features are transformed into positive and negative point prompts, enabling the Segment Anything Model (SAM) to produce precise nuclear delineations without any parameter updates. Extensive experiments across multiple histopathology benchmarks demonstrate that SPROUT achieves competitive performance without supervision or retraining, establishing a novel paradigm for scalable, training-free nuclear instance segmentation in pathology.

Github: https://github.com/Y-Research-SBU/SPROUT **Correspondence:** Chenyu You: chenyu.you@stonybrook.edu

Date: November 26, 2025

1 Introduction

Nuclear instance segmentation delineates individual nucleus for systematic downstream analysis (Caicedo et al., 2019; Greenwald et al., 2022; Gupta et al., 2023) and advances cancer prognosis, diagnosis, and treatment (Madabhushi and Lee, 2016; Lu et al., 2018; Pinckaers et al., 2021; You et al., 2025). In histopathology, cellular structure visualizations are most commonly obtained from hematoxylin and eosin (H&E) staining (Vahadane et al., 2016). Hematoxylin highlights nuclei in dark blue or purple and eosin stains cytoplasm and extracellular components in pink for separation (Ruifrok et al., 2001). However, the intrinsic properties of pathology images pose unique challenges for instance segmentation. First, the narrow color spectrum and staining variability limit robust visual cues. Second, a single patch can contain thousands of densely packed nuclei with weak boundaries. Third, pixel-wise annotations are scarce and labor-intensive for pathologists.

To address these challenges, numerous specialized nuclear segmentation networks have been explored under varying levels of supervision, including fully-supervised (Graham et al., 2019; Qu et al., 2019; He et al., 2021b; You et al., 2022b, 2023d; Chen et al., 2023a; He et al., 2023), semi-supervised (Zhou et al., 2020; Wu et al., 2022; You et al., 2022c,a,d, 2023a,b, 2024; Jin et al., 2022), weakly-supervised (Zhao and Yin, 2020; Nishimura et al., 2021; Liu et al., 2022), and self-supervised (Sahasrabudhe et al., 2020; You et al., 2020; Xie et al., 2020). Nevertheless, their performance is often limited when facing distribution shifts, varying annotation protocols, and restricted training data (Pachitariu and Stringer, 2022). Together, these limitations underscore the need for generalizable and robust approaches to nuclear instance segmentation.

Vision foundation models mark a turning point in image segmentation. Segment Anything Model (SAM) (Kirillov et al., 2023) achieves robust zero-shot, class-agnostic segmentation by leveraging large-scale training on the SA-1B datasets. Building on SAM, subsequent work has explored fine-tuning (Zhang et al., 2024c; Ma

¹Stony Brook University, ²Johns Hopkins University

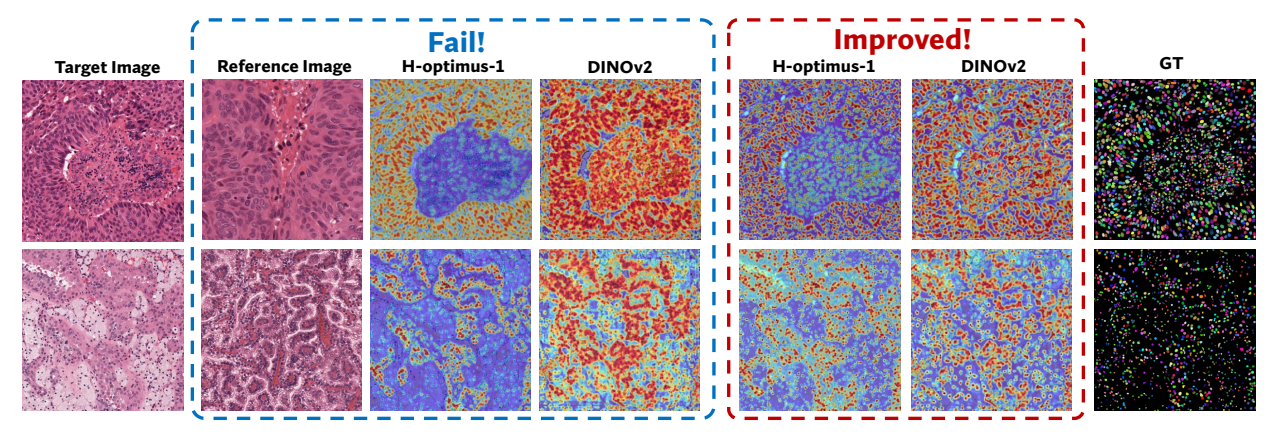


Figure 1 Comparison of one-shot and proposed self-reference strategies in feature extraction. One-shot (blue box) fails to capture precise and diverse nuclei, even with similar pairs or backbones trained on natural and pathology images. Instead, our self-reference approach (red box) leverages high-confidence regions within the image to extract more robust features for similarity guidance.

et al., 2024; Peng et al., 2024; Archit et al., 2025) and adapter-based strategies (Chen et al., 2023b; Na et al., 2024; You et al., 2023c; Cheng et al., 2024; Chen et al., 2025a) to accommodate SAM to medical objectives. However, the need for substantial annotations and resource-intensive training constraints their practicality in pathology.

An appealing alternative is to transform feature correspondences between the annotated references and targeted images into actionable prompts (Liu et al., 2024; Zhang et al., 2024a; Liu et al., 2025) without supervision or retraining. One might reasonably expect obtaining high-quality prompts from external backbones trained on natural or pathological domains, such as DINOv2 (Oquab et al., 2024) and H-optimus-1 (Bioptimus, 2025). Yet the distinct properties of pathological images hinder such direct transfer. As illustrated in Figure 1, even when target and reference pairs are carefully matched in color, nuclear size, and spatial distribution, backbone models exhibit characteristic failures. Feature extractors trained on natural images can over-amplify the nuclear regions, while pathology-trained ones still struggle to capture subtle, heterogeneous cell-level features. Unlike natural images with a limited number of salient objects occupying large portions, nuclei are harder to capture reliably due to their fine-grained structures, which may consist of only a few thousand pixels. Moreover, few-shot strategies are often impractical in pathology. Variations in staining, cellular density, and local morphology preclude the establishment of appropriate references or consistent image matching. Consequently, their unstable performance across references is unsuitable for practical deployment.

In this work, we address these challenges by introducing SPROUT (Stain Priors with pRototypical partial Optimal transport for Unlabeled prompTing), a novel prompting framework that guides SAM in nuclear instance segmentation without any training. Specifically, we leverage the biochemical affinity of H&E staining to generate high-confidence foreground and background regions, from which semantically reliable prototypes are extracted to inform global feature allocation. Such a self-reference strategy is notably effective as these prototypes calibrate image-specific feature activations for precise and complete nuclear delineation, as illustrated in Figure 1. To achieve comprehensive coverage of the cells and mitigate ambiguity, we propose POT-Scan, a principled progressive partial optimal transport scheme built on feature-prototype similarity mapping. In addition, we incorporate biological priors into a containment-aware Non-Maximum Suppression (NMS) strategy for SAM prediction refinement. We empirically validate our SPROUT across three benchmark datasets, i.e., MoNuSeg (Kumar et al., 2017), CPM17 (Vu et al., 2019), and TNBC (Naylor et al., 2018), and demonstrate remarkable performance compared with SAM-based, fully-supervised, and weakly-supervised counterparts while remaining computationally efficient. Our main contributions are summarized as follows:

• To the best of our knowledge, SPROUT is the **first** fully training-free framework for nuclear instance segmentation in H&E pathology images without annotations. By addressing the limitations of reference-based methods, we introduce a novel self-reference mechanism that offers a lightweight yet generalizable solution to domain gaps.

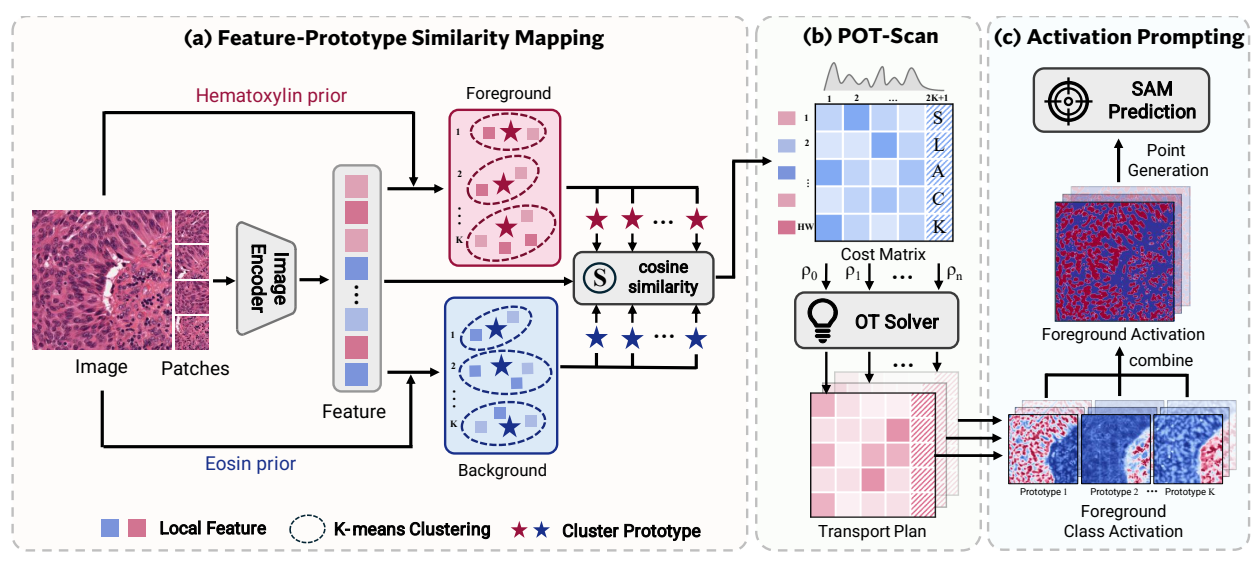


Figure 2 SPROUT pipeline for point prompt generation. It consists of three steps: (i) Feature–prototype similarity mapping: H&E stain priors are used to identify high-confidence foreground and background regions, from which clustering extracts representative prototypes that serve as anchors for similarity matching; (ii) POT-Scan: a partial optimal transport scheme that progressively aligns features to prototypes, filtering ambiguous assignments through partial mass transport; (iii) Activation prompting: prototype-reweighted activations are aggregated into foreground maps, from which positive and negative point prompts are sampled to guide SAM-based instance prediction.

- We propose POT-Scan, a principled scheme with theoretical guarantees that adaptively balances nuclear coverage and noise suppression. Our quantitative and qualitative analyses further elucidate the intrinsic behavior of prompt generation and verify its robust performance under diverse hyperparameter settings.
- Across three challenging benchmarks, SPROUT consistently achieves remarkable performance gains (+8.2% AJI on MoNuSeg). These results highlight the potential of robust prompt generation and patch-based decomposition to unlock the zero-shot capabilities of vision foundation models in histopathology.

2 Related Works

Prompt Engineering for SAM. SAM (Kirillov et al., 2023), as a vision foundation model, enables zero-shot and class-agnostic segmentation via point, box, and coarse mask prompts. However, its performance in precise object delineation heavily depends on the prompt accuracy and placement. This has spurred a growing body of work on automatic prompt generation, as large-scale manual guidance is impractical in real-world clinical settings. Recent work includes embedding-oriented prompt representation learning (Luo et al., 2023; Yue et al., 2024; Li et al., 2025; Yan et al., 2025), detector-based prompt generation (Wu et al., 2023; Zheng et al., 2024; Xie et al., 2025), and heuristic-driven approaches (Gao et al., 2024). Meanwhile, prototype-guided methods (Zhang et al., 2024c; Wang et al., 2025) exploit feature correspondences between reference and target images to improve representation learning. Building on this idea, several training-free approaches generate prompts directly from such similarity mapping in natural images (Zhang et al., 2024a; Liu et al., 2024) and medical images (Liu et al., 2025). However, these methods are typically designed for few-object scenarios and rely on carefully curated reference images. By contrast, nuclear segmentation presents a more challenging setting, involving thousands of densely packed and morphologically diverse objects within a single image. These limitations highlight the need for new strategies that can generate reliable prompts without external references while remaining computationally efficient.

Nuclear Instance Segmentation. Fully supervised nuclear instance segmentation approaches can be broadly grouped into three categories: contour-based (Chen et al., 2016), distance-mapping (Graham et al., 2019; He et al., 2021a), and detection-based (Jiang et al., 2023). While effective, these methods heavily rely on dense pixel-level annotations, which are costly and time-consuming. Semi- and weakly-supervised alternatives, particularly point-supervised approaches, have been explored as a new direction by transforming

sparse labels into coarse pixel-level cues, such as Voronoi-based (Tian et al., 2020) or pseudo-edge maps (Yoo et al., 2019). But these approaches still suffer from unreliable pseudo masks and fail to adequately separate overlapping nuclei. With the advent of SAM, adapting foundation models to medical imaging has become a prominent direction. Methods such as MedSAM (Ma et al., 2024) and fine-tuning variants (Huang et al., 2024a,b) still require additional annotations and incur substantial computational overhead. To alleviate these constraints, other studies, including PromptNucSeg (Shui et al., 2024), UN-SAM (Chen et al., 2025b), and All-in-SAM (Cui et al., 2024), attempt to reduce these costs by training auxiliary prompters, introducing domain-adaptive feature tokens, or fine-tuning from self-generated masks. Building on these, we argue that competitive segmentation performance can be attained directly from SAM through proper prompt design and appropriate patch granularity without altering the model architecture.

3 SPROUT

The pipeline comprises three steps: (i) feature—prototype similarity mapping (Section 3.1), (ii) partial optimal transport scan with activation prompting (Section 3.2), and (iii) instance mask prediction with refinement (Section 3.3). As shown in Figure 2, SPROUT leverages stain priors to construct robust self-reference features, aligns them with semantically reliable prototypes through a theoretically grounded POT-Scan, and generates precise point prompts to guide SAM without additional training. The following subsections describe each stage in detail. The detailed theoretical analysis is provided in Appendix A.

3.1 Feature-prototype Similarity Mapping

The first step is to extract self-reference features from stain priors and condense them into representative prototypes for subsequent matching. Given an image $I \in \mathbb{R}^{H \times W \times 3}$, we partition it into n overlapped patches, denoted as $\{I^i\}_{i=1}^n$. Each patch is encoded as $F^i = f_{\theta}(I^i)$, where f_{θ} denotes the pretrained encoder. Patchlevel features are stitched to reconstruct a global representation $F \in \mathbb{R}^{h \times w \times d}$, where (h, w) is the spatial resolution of the encoded feature map and d is the embedding dimension.

To derive self-reference masks, we first condition on stain color priors by transforming images into optical density space: $OD = -\log(x/x_0)$, where x is the observed RGB intensity and x_0 is the reference intensity. Using the normalized stain matrix $Q = [Q_H, Q_E]$, the concentration map $S = [S_H, S_E]^{\top}$ is obtained via linear decomposition: $S = Q^+ \cdot OD$, where Q^+ is the pseudoinverse. A visual illustration is provided in Appendix B.4. Otsu's thresholding (Appendix B.8) is then utilized to separate coarse foreground and background regions. Within each region, pixels with the top t stain intensities are selected to construct high-confidence masks M_{fg} and M_{bg} for self-reference. To ensure the spatial correspondence, we resize the pixel-level masks to feature resolution and overlap them for prototype extraction. Each class-specific feature set is then clustered into K groups using K-means to derive representative prototypes $\mathcal{P}_c = \{P_c^1, \ldots, P_c^K\}$:

$$\mathcal{P}_c = \underset{\{P_c^1, \dots, P_c^K\}}{\text{arg min}} \sum_{p \in \Omega} M_c(p) \underset{k=1, \dots, K}{\text{min}} ||F(p) - P_c^k||^2,$$
(1)

where $c \in \{fg, bg\}$, $M_c \in \{0, 1\}$, and Ω denotes the feature map spatial locations. The resulting prototypes $\{\mathcal{P}_{fg}, \mathcal{P}_{bg}\}$ capture the global semantic feature characteristics of foreground and background, serving as class-specific anchors for subsequent mapping.

3.2 POT-Scan and Activation Prompting

How can we reliably propagate prototype semantics to all features when isolated point-wise assignments are unstable and collapse-prone in the presence of noise? Given the intra-class variability of foreground and background features, a distribution-level formulation that allocates features across prototypes is needed.

Preliminary. Optimal transport (OT) seeks the minimal-cost mapping between distributions under marginal constraints, providing a principled measure of distributional discrepancy. Given probability vectors $\mu \in \mathbb{R}^{n \times 1}$, $\nu \in \mathbb{R}^{m \times 1}$ with cost matrix $C \in \mathbb{R}^{n \times m}_+$, the Kantorovich formulation (Kantorovich, 1942) solves:

$$\min_{T \subset \mathbb{D} \times m} \langle T, C \rangle_F, \quad \text{s.t. } T \mathbf{1}_m = \mu, \ T^{\top} \mathbf{1}_n = \nu, \tag{2}$$

where T is the transport plan and $\langle \cdot, \cdot \rangle_F$ denotes the Frobenius inner product. Relaxing the marginal constraints with divergences yields unbalanced OT. Adding entropic regularization (Cuturi, 2013) enables efficient solutions via the Sinkhorn-Knopp algorithm (Knight, 2008). Further background, OT variants, and solver details are in Appendix A.1 and A.2.

POT-Scan. While OT offers a principled formulation, assigning features to prototypes in pathology is challenging due to noise and ambiguity. A naïve approach is to match features to their nearest prototypes via cosine similarity:

$$C = 1 - \frac{\tilde{F}P^{\top}}{||\tilde{F}||_2||P||_2},\tag{3}$$

where $P \in \mathbb{R}^{2K \times d}$ is the prototype matrix and $\tilde{F} \in \mathbb{R}^{hw \times d}$ is the flattened feature map. However, standard OT requires full mass transport, and even its unbalanced variant still imposes penalties for discarding noisy features. To address this, we adopt **partial OT**, which allows a fraction of the mass to remain unmatched and naturally filters ambiguous regions (Appendix A.3). Formally, transporting a fraction $\rho \in (0,1]$ of the mass is posed as:

$$\min_{T \in \Pi} \langle T, C \rangle_F + \lambda K L(T^{\top} \mathbf{1}_N || \frac{\rho}{M} \mathbf{1}_M),$$
s.t. $\Pi = \{ T \in \mathbb{R}_+^{N \times M} | T \mathbf{1}_M \le \frac{1}{N} \mathbf{1}_N, \ \mathbf{1}_M T^{\top} \mathbf{1}_N = \rho \}$

where $N=h\times w$ denotes the number of source features, assumed to follow a uniform mass distribution since each feature is equally weighted, and M=2K is the number of target prototypes. This leads to our POT-Scan, where the transport ratio ρ is progressively increased: starting from a small initial value ρ_0 that favors easy feature–prototype matches and gradually incorporating more ambiguous features until a stopping criterion is met.

Although conceptually intuitive, Eq.(4) cannot be solved directly using standard scaling algorithms due to non-normalized constraints. Following the reformulation of (Zhang et al., 2024b), we append a slack column to absorb the residual $1 - \rho$ mass, thereby restoring normalized marginals and enabling efficient Sinkhorn-based optimization. Detailed proofs, solver derivation, and corresponding pseudo-code are provided in Appendix A.3, A.4, and A.5.

Activation Prompting. Given optimal transport plan T^* , features are reweighted as $F^* = \tilde{F} \odot T^* \in \mathbb{R}^{hw \times 2K}$. These are mapped back to the image space via the resizing operator \mathcal{R} and refined with DenseCRF, producing activation maps $F' = \text{CRF}(\mathcal{R}(F^*)) \in \mathbb{R}^{H \times W \times 2K}$. Foreground and background activations are aggregated as $[F'_{fg}, F'_{bg}] = [\sum_k F'^k_{fg}, \sum_k F'^k_{bg}]$, which are then binarized using Otsu's thresholding. Combining these with the initial high-confidence masks yields positive points through a watershed-based procedure (Appendix B.8), while negative points are uniformly sampled from expanded background masks with an additional stride to ensure coverage. The process terminates once multiple regions merge into a large connected component, as further expansion risks conflating distinct nuclei. This balances robust assignments with the gradual inclusion of difficult features, resulting in stable and informative prompts for SAM.

3.3 Instance Mask Prediction and Refinement

The final step is to generate instance-level nuclear masks from activation-derived prompts and refine them to correct boundary errors from overlapping cells and weak edges. To capture fine-grained nuclear structures, we perform inference at the patch level, which allows SAM to better localize individual nuclei. Positive and negative prompts further help separate closely packed nuclei from surrounding tissue (Detailed illustrations are in Appendix E.1). When a nucleus has multiple positive cues, each positive together with y nearest negatives is provided to SAM within its patch, and highly overlapped predictions are merged. Although weak inter-nuclear boundaries may lead to adjacent nuclei being predicted into a single instance, fragmentation is rare due to their homogeneous interiors. To this end, we introduce containment-aware non-maximum suppression (NMS) that penalizes large masks enclosing multiple smaller nuclei. Specifically, we apply a tanh-based decay penalty proportional to the number of contained instances and combine SAM's confidence S_{SAM} with the normalized hematoxylin-channel response S_H' into a unified score $S_{\text{SAM}} + S_H'$ for filtering. This complementary strategy leverages both morphological consistency and biological priors, suppressing

Table 1 Performance evaluations of nuclear instance segmentation. We benchmark methods across fully-, weakly-, and self-supervised, and SAM- approaches on MoNuSeg and CPM17 datasets. Segmentation performance is reported using AJI (\uparrow) , PQ (\uparrow) , DQ (\uparrow) , SQ (\uparrow) , and Dice (\uparrow) . Best results are highlighted in **bold**, and second-best are underlined.

Method	SAM	Supervision]	MoNuSe	g			CPM17			
Method	SAM	Supervision	AJI	PQ	$\mathbf{D}\mathbf{Q}$	\mathbf{SQ}	Dice	AJI	\mathbf{PQ}	$\mathbf{D}\mathbf{Q}$	\mathbf{SQ}	Dice
U-Net _{MICCAI'15}	×	fully	0.421	0.403	0.571	0.705	0.635	0.554	0.527	0.718	0.734	0.741
$\rm SPN{+}IEN_{ISBI'22}$	×	point	0.521	0.436	0.661	0.660	0.677	0.540	0.485	0.695	0.699	0.701
$SC-Net_{MEDIA'23}$	×	point	0.539	0.450	0.648	0.694	0.732	0.561	0.486	0.692	0.703	0.698
$SAM_{CVPR'23}$	✓	point*	0.061	0.262	0.384	0.751	0.353	0.135	0.469	0.601	0.781	0.329
DES - $SAM_{MICCAI'24}$	✓	box	0.463	0.429	0.621	0.691	0.672	0.512	0.517	0.735	0.704	0.688
$MedSAM_{Nat.\ Commun.'24}$	✓	box*	0.502	0.327	0.514	0.752	0.687	0.648	0.559	0.788	0.706	0.793
$UN\text{-}SAM_{\mathrm{MEDIA'25}}$	✓	fully	0.482	0.477	0.656	0.728	0.792	0.581	0.574	0.734	0.782	0.795
$Med\text{-}SA_{MEDIA'25}$	✓	fully	0.511	0.493	0.679	0.727	0.772	0.565	0.564	0.731	0.772	0.806
$COIN_{ICCV'25}$	✓	$unsupervised^{\dagger}$	0.519	0.410	0.581	0.706	0.748	0.572	0.515	0.690	0.746	0.778
SPROUT	✓	${\rm training\text{-}free}^{\dagger}$	0.621	0.601	0.817	0.736	0.795	0.662	0.616	0.796	0.774	0.821

^{*} indicates baseline evaluation of the foundation models, and the supervision column specifies the input prompt type. † denotes no ground truth used.

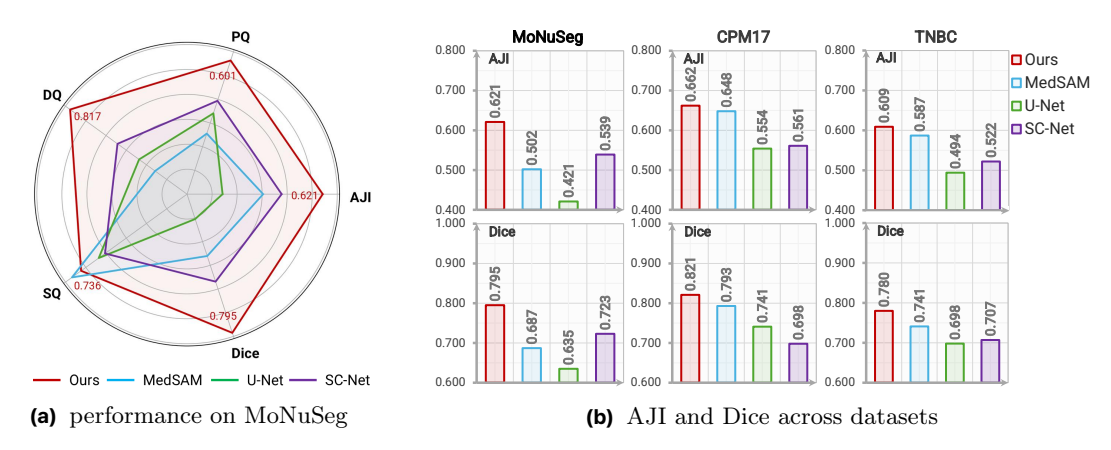


Figure 3 Performance comparison across supervision types. SPROUT consistently outperforms SAM-based (MedSAM), fully supervised (U-Net), and point-supervised (SC-Net) models across datasets with superior effectiveness in segmentation.

false positives and improving boundary delineation. Further implementation details of containment-aware NMS are provided in Appendix D.4.

4 Experiments and Results

We evaluate SPROUT on three benchmark datasets, MoNuSeg (Kumar et al., 2017), CPM17 (Vu et al., 2019), TNBC (Naylor et al., 2018), and PanNuke (Gamper et al., 2020) using instance-level metrics (AJI, PQ, DQ, SQ) and the semantic-level Dice coefficient. Complete dataset statistics and metric definitions are provided in Appendix B.1 and B.2. Section 4.1 reports comparisons with state-of-the-art nuclear instance segmentation methods, and Section 4.2 (with Appendix D) presents ablations that validate the key components of SPROUT. We further analyze robustness through hyperparameter sensitivity studies (Section 4.3). Additional implementation details are included in Appendix B.3.

4.1 Main Results

Comparison with Baselines. We benchmark our method against other state-of-the-art approaches in nuclear instance segmentation, including U-Net (Ronneberger et al., 2015), SPN+IEN (Liu et al., 2022), SC-Net (Lin et al., 2023), SAM (Kirillov et al., 2023), MedSAM (Ma et al., 2024), UN-SAM (Chen et al., 2025b), DES-SAM (Huang et al., 2024a), Med-SA (Wu et al., 2025), COIN Jo et al. (2025). As summarized in Table 1, our method achieves the highest AJI and Dice scores and consistently outperforms all counterparts

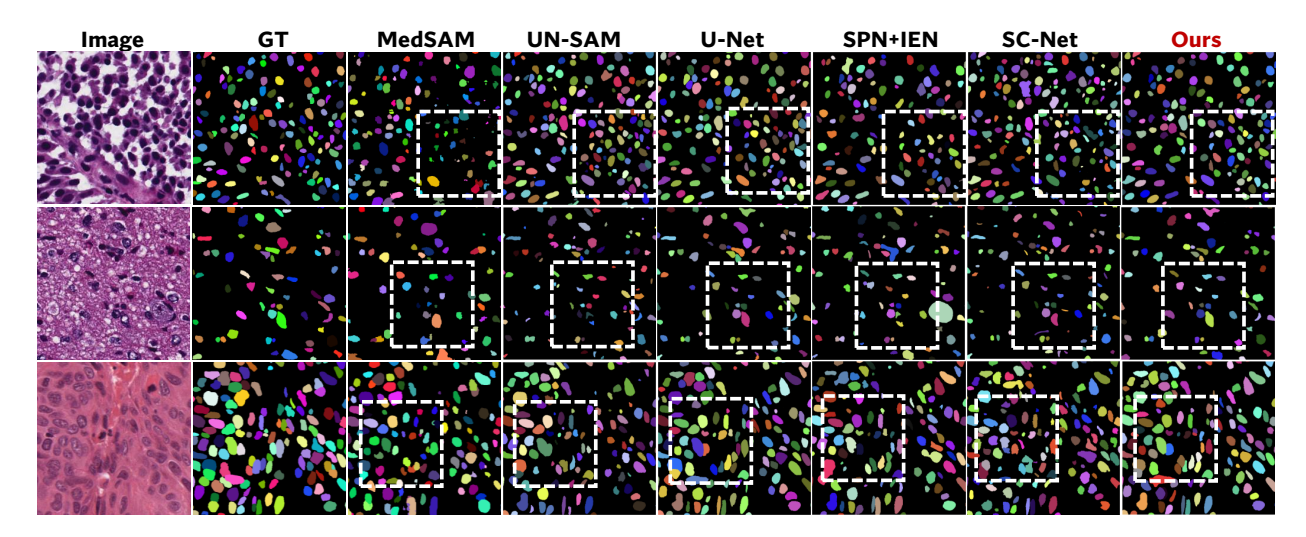


Figure 4 Visualization of instance segmentation results from different methods. SPROUT delivers more correct instances with fewer overlaps. The highlighted regions show distinct differences.

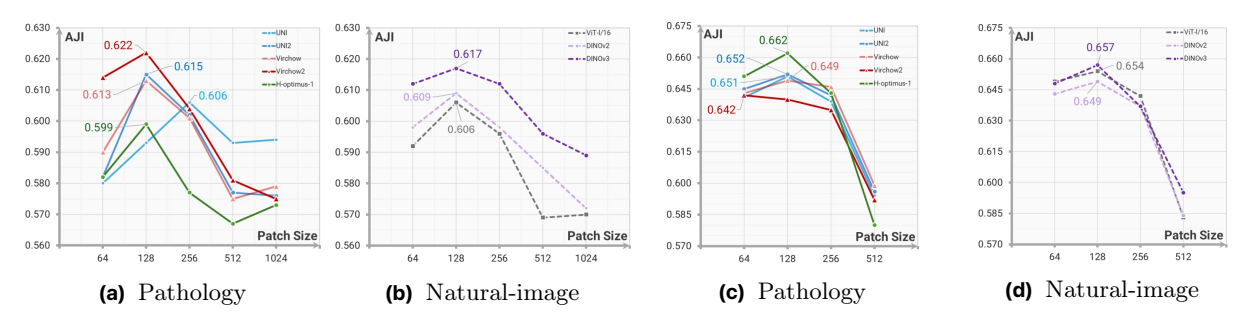


Figure 5 Performance comparison of pathology-based and natural-image-based backbones. On MoNuSeg (a, b) and CPM17 (c, d), the self-reference mask strategy mitigates the domain gap and achieves the best AJI at patch size 128×128 matching nuclear scale.

with up to 8.2% absolute gains in AJI on the challenging MoNuSeg dataset. Notably, the PQ scores of 0.601 on MoNuSeg and 0.616 on CPM17 demonstrate its strong ability to maintain object-level consistency. The baseline descriptions and reproduction details are provided in Appendix B.6. Comparative segmentation visualizations from natural-image segmentation models are provided in Appendix C.2 to highlight their limitations in pathology.

Analysis by Supervision Type and Visualization. Figure 3 shows our method surpasses MedSAM, U-Net, and SC-Net from different supervision regimes without annotations and training. We further make a visual comparison in Figure 4. SPROUT produces clean, non-overlapping masks in challenging cases with nuclei-tissue color similarity or light stain. By automatically generating smart positive—negative to constrain predictions, SPROUT fully exploits SAM's capacity and demonstrates strong generalizability and robustness across datasets and background appearances. Meanwhile, it offers an efficient alternative to supervised approaches, making training-free and annotation-free on pathological images possible while still achieving superior instance- and semantic-level accuracy. Additional qualitative examples across datasets are provided in Appendix C.1.

4.2 Ablation Studies

We conduct ablation studies to evaluate the core components of SPROUT, focusing on two key questions: (i) How does SPROUT generate reliable point prompts for SAM prediction effectively? (ii) Which post-processing strategy ensures accurate instance mask selection?

Feature Extractors. To assess the effect of the proposed self-reference mask strategy, we evaluate

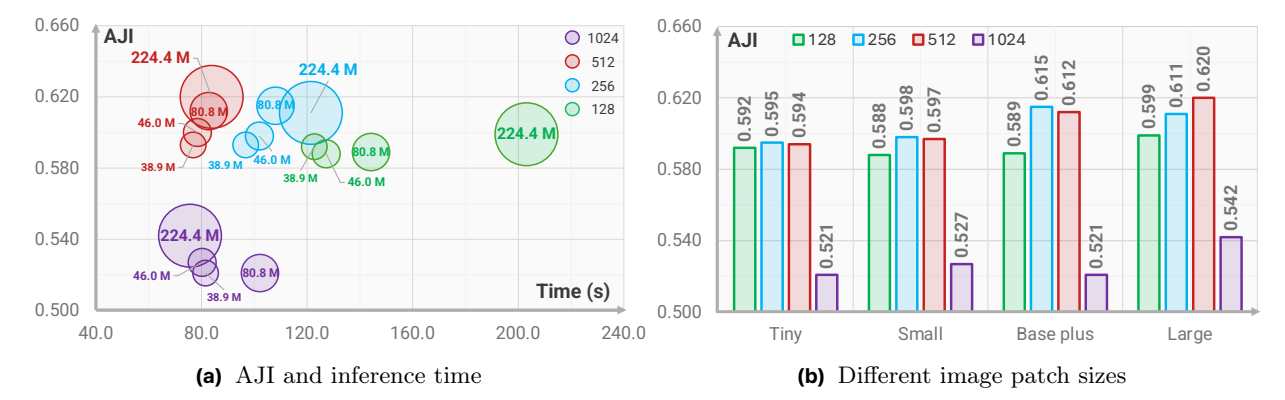


Figure 6 Relationship between SAM variants and patch size. Appropriate patch sizes narrow the performance gap between large and small SAM variants and enable flexible deployment across resource settings. The best performance is obtained with the large SAM at patch size 512×512 . Results are reported on the MoNuSeg dataset with a fixed patch overlap ratio of 0.5.

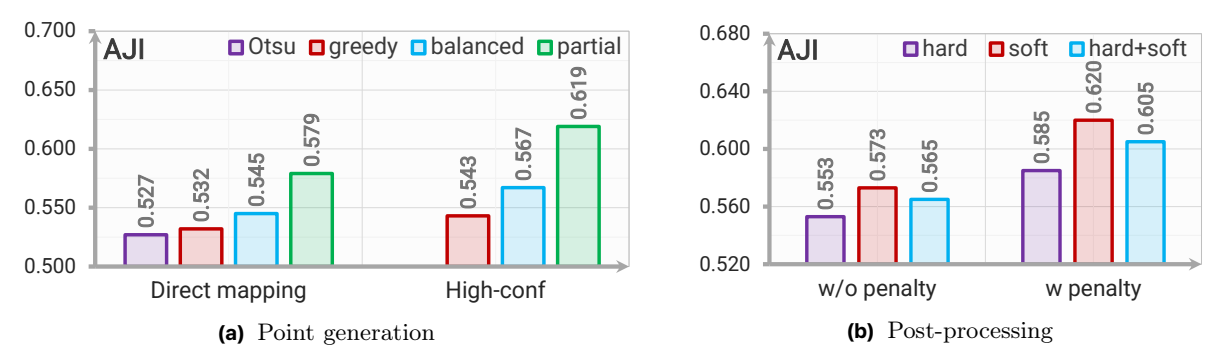


Figure 7 (a) High-confidence masks yield cleaner reference features with modest gains. Partial OT outperforms balanced OT by enabling more flexible assignments. (b) Adding a containment-aware penalty consistently improves AJI across NMS types. Soft NMS achieves the best performance by allowing mild overlap, which better matches practical morphology.

feature extractors trained on both pathology (UNI, UNI2 (Chen et al., 2024), Virchow (Vorontsov et al., 2024), Virchow2 (Zimmermann et al., 2024), H-optimus-1 (Bioptimus, 2025)) and natural images (ViT-1/16 (Dosovitskiy et al., 2020), DINOv2 (Oquab et al., 2024), DINOv3 (Siméoni et al., 2025)) using the MoNuSeg and CPM17 datasets. The Appendix B.7 provides further details on each backbone. As shown in Figure 5, both types of backbones yield comparable AJI scores, typically within 1%. Virchow2 and DINOv3 achieve the best performance on MoNuSeg, while H-optimus-1 and DINOv3 perform best on CPM17. These findings validate that the proposed self-reference strategy incorporates image-specific H&E color priors to refine scales and allows cross-domain transfer without specialized fine-tuning. The consistent peaks of AJI at a patch size of 128×128 align with the feature extractor's receptive field relative to cell sizes. Overly large patches (≥ 512) dilute nuclear signals and overly small ones risk fragmenting them. Additional cross-dataset results demonstrating the robustness of self-reference are included in Appendix D.2.

SAM Variants. Since SPROUT relies on SAM for instance generation, we analyze how model size influences segmentation. Figure 6 reports AJI for large, base-plus, small, and tiny variants under different patch sizes. Splitting images into moderate patches improves AJI relative to whole-image input, while overly small patches provide little gain and increase computational cost by fragmenting context and amplifying noise. Large and base-plus models perform best, but the advantage of large over base-plus is minor since nuclei within each patch are relatively homogeneous. Smaller variants also remain competitive with patch inputs, suggesting practical value in resource-limited settings.

Point Generation. In Figure 7a, direct Otsu-based foreground-background separation serves as the color-only baseline and shows its limitation under noise. High-confidence filtering improves robustness by removing unreliable regions. Building on similarity-based feature extraction, greedy mapping yields modest

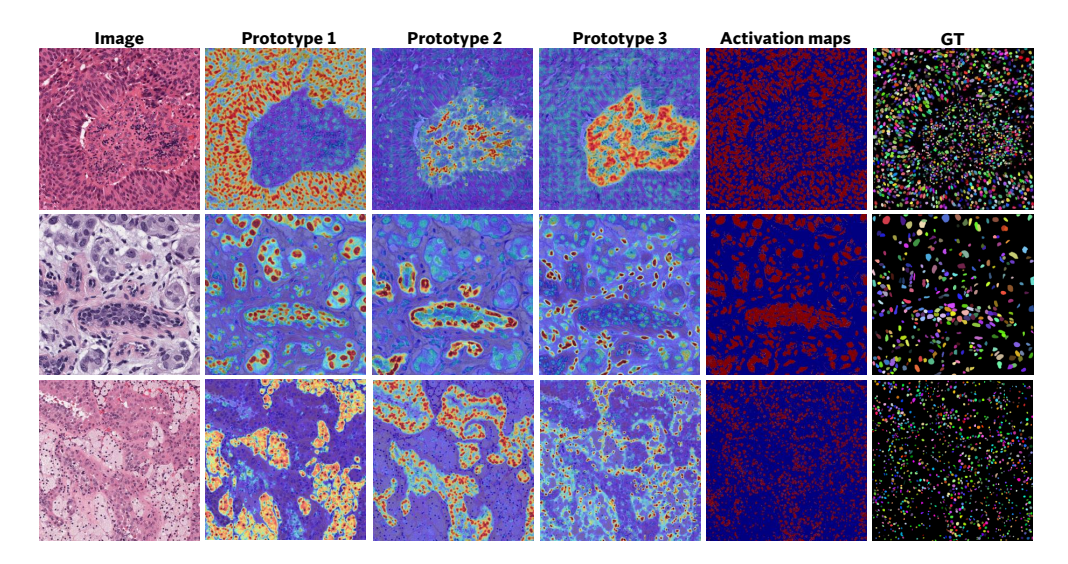


Figure 8 Visualization of class activation (MoNuSeg). Different prototypes emphasize complementary tissue morphologies, with their aggregation aligning with the ground truth. Clustering-based prototypes capture diverse feature variations for accurate localization.

gains, since the locally determined features are easily perturbed by noise. Balanced OT offers marginal improvement as it enforces the assignment of ambiguous pixels to prototypes. In contrast, partial OT delivers the best performance by transporting low-cost, high-confidence matches, leaving uncertain regions in the slack column. See Appendix B.5 and D.3 for detailed runtime evaluation, comprehensive quantitative results, and an extended point quality analysis.

Post-processing. Figure 7b compares different NMS strategies with and without the containment-aware penalty. Without the penalty, large masks containing multiple nuclei are often retained, as their low IoU with smaller nucleus masks prevents them from being identified as redundant during NMS. Introducing the penalty improves AJI by about 5%, explicitly discouraging such scenarios. Among the selection strategies, soft

Figure 9 Average runtime per image and per nucleus. Perimage runtime is measured without parallelization. Wall-clock time uses 4-way parallel processing. The H-optimus-1 backbone and large SAM weight are employed.

Metric	MoNuSeg	CPM17	TNBC
time/image (s)	170.651	9.452	8.305
wall-clock/image (s)	49.343	2.658	2.449
time/nucleus (ms)	282.232	78.869	103.091

NMS achieves the best balance by reducing redundant overlaps while still allowing partial overlap in dense regions, consistent with the biological reality of clustered nuclei. The hybrid strategy is less suitable because it enforces strict separation rather than acceptable overlaps. Ablations of soft NMS decay functions and score strategies are in Appendix D.4.

Class Activation. Figure 8 illustrates the prototype activation after POT-scan. Each prototype emphasizes distinct morphological patterns, and their combination recovers foreground structures closely aligned with ground truth. This confirms that K-means clustering of features produces discriminative prototypes, enabling robust capture of nuclei even under subtle feature diversity.

Feature Embeddings. Despite the class activation map provides a spatial view, it does not reveal their underlying distribution. To concretely analyze how POT-Scan reshapes the embedding space, we perform UMAP to the raw and the transported features, as shown in Figure 10. Before POT-Scan, the foreground and background embeddings are highly mixed, indicating that raw encoder features alone do not produce well-separated clusters due to staining variability and weak nuclear boundaries. After POT-Scan, the transported features exhibit clearer separation into compact foreground and background groups around prototypes, while those mapped to the slack column lie between the two classes, suggesting ambiguous or noisy regions and demonstrating improved feature assignment. Assigning these uncertain features to slack, rather than forcing them into certain classes, improves the reliability of activation maps used for prompt generation.

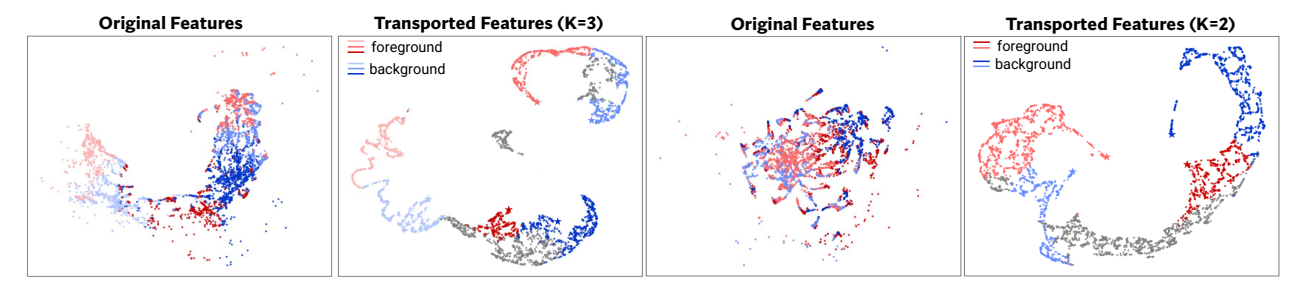


Figure 10 UMAP visualization of feature embeddings before and after POT-Scan. Red and blue denote foreground and background features, respectively. Grey points indicate features assigned to the slack column, which are ultimately treated as background. Stars are the prototypes. K denotes the number of cluster centers per class used in the K-means prototype construction.

Runtime Analysis. To assess the practical deployability of our approach, we examine its runtime characteristics as summarized in Table 9. The CPM17 and TNBC images can be fully processed within 10 seconds, and the more challenging MoNuSeg dataset requires less than one minute per image without any hardware-level optimization. In real use, however, the system leverages multi-thread parallelism, allowing images to be processed concurrently. On a single RTX 4090 GPU with four parallel threads, the wall-clock time per image is dramatically reduced. It is important to note that the reported per-nucleus time is measured without parallelization and therefore should not be interpreted as practical per-instance latency. Actual throughput is governed by the wall-clock image time, which more accurately reflects the method's deployable performance and can be further shortened by adopting lighter-weight SAM variants. Detailed point-generation process runtime is provided in Appendix B.5.

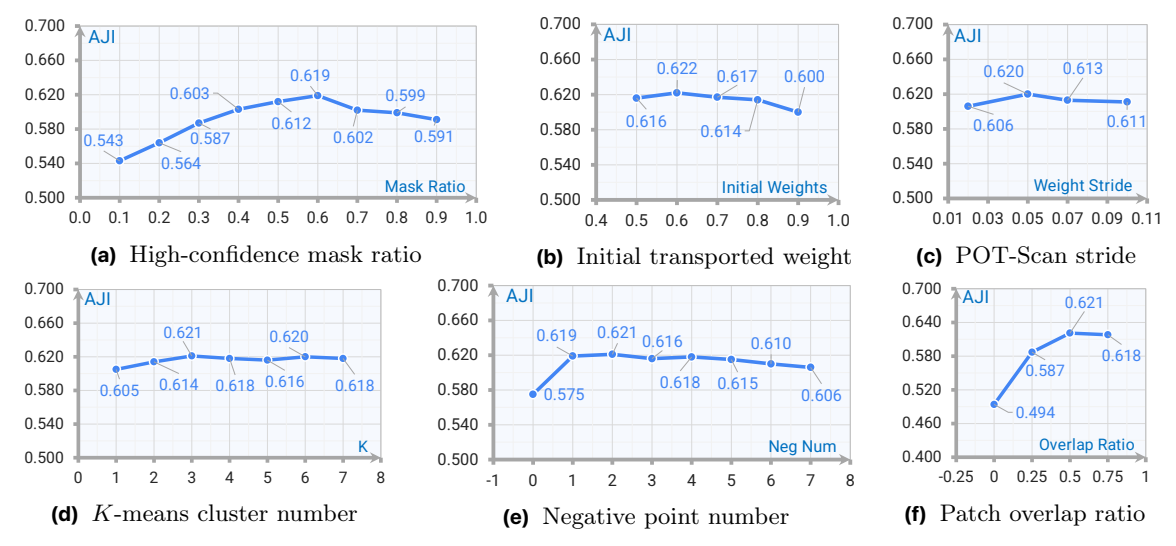


Figure 11 Hyperparameter sensitivity analysis (MoNuSeg). We evaluate AJI across six representative parameters. Minor variation (less than 3%) are observed under wide changes, confirming SPROUT's robustness to hyperparameter choices with minimal tuning.

4.3 Sensitivity Analysis

We analyze the impact of key hyperparameters on segmentation performance to better understand SPROUT's behavior under different configurations. Figure 11 reports results for point generation and mask prediction stages. Across all settings, SPROUT remains stable, with performance varying by less than 3% except for extreme parameters. This robustness indicates that the framework requires little hyperparameter tuning in practice. Experimental details are provided in Appendix B.3.

Point Generation. In Figure 11a and 11b, the high-confidence mask ratio peaks around 0.6 and decreases as it approaches 1. This indicates that a moderate ratio balances reliable regions with sufficient coverage,

while extreme values either lack generalization or introduce noise. A similar trend is observed for the initial transported weight. The stride used in POT-Scan is relatively milder in Figure 11c. Small strides cause the process to stop early when nuclei are densely packed, while large strides may skip fine details. For the number of K-means clusters, small values fail to capture the diversity of foreground and background features. Performance improves as the cluster number increases and stabilizes once $K \geq 3$, as shown in Figure 11d.

Mask Prediction. In Figure 11e, introducing a small number of negative points improves accuracy by excluding ambiguous regions that a single positive point cannot separate, as illustrated in Appendix E.1. However, too many negative prompts make the model conservative, leading to smaller and fragmented predictions. The prediction patch overlap ratio has the strongest impact in this stage, as in Figure 11f. Without overlap, AJI is low due to border artifacts. Moderate overlap around 0.5 is critical for handling boundary regions, while avoiding redundant computation.

5 Conclusion

We presented SPROUT, a fully training-free framework for nuclear instance segmentation that generates prompts automatically without annotations. SPROUT introduces a self-reference strategy and a theoretically-grounded POT-Scan scheme to achieve precise feature representation and reduce domain gaps. By guiding SAM with automatically generated point prompts and applying a containment-aware NMS for lightweight refinement, SPROUT yields accurate and efficient segmentation without needs for fine-tuning or adapter modules. Extensive experiments show that SPROUT outperforms previous state-of-the-art methods across multiple datasets and provides new insights into the behavior of prompting-based pipelines. Beyond nuclear segmentation, this work points toward broader potential of bridging domain gaps via cross-domain priors, offering a path to more robust and adaptable medical imaging models. As elaborated in Appendix F, the framework generalizes to other nuclear imaging modalities with a slight modification of the modality-specific foreground priors. We further showcase a conceptual extension to fluorescent microscopy, where SPROUT produces high-quality nuclei delineations on the DSB2018 dataset (Caicedo et al., 2019). These observations underscore SPROUT's prospects as a promising, scalable, and trustworthy step toward reliable, end-to-end AI integration in digital pathology.

References

Anwai Archit, Luca Freckmann, Sushmita Nair, Nabeel Khalid, Paul Hilt, Vikas Rajashekar, Marei Freitag, Carolin Teuber, Melanie Spitzner, Constanza Tapia Contreras, et al. Segment anything for microscopy. *Nature Methods*, 22(3):579–591, 2025.

Jean-David Benamou, Guillaume Carlier, Marco Cuturi, Luca Nenna, and Gabriel Peyré. Iterative bregman projections for regularized transportation problems. SIAM Journal on Scientific Computing, 37(2):A1111-A1138, 2015.

Bioptimus. H-optimus-1. https://huggingface.co/bioptimus/H-optimus-1, 2025. Software.

Luis A Caffarelli and Robert J McCann. Free boundaries in optimal transport and monge-ampere obstacle problems. Annals of Mathematics, pages 673–730, 2010.

Juan C Caicedo, Allen Goodman, Kyle W Karhohs, Beth A Cimini, Jeanelle Ackerman, Marzieh Haghighi, CherKeng Heng, Tim Becker, Minh Doan, Claire McQuin, et al. Nucleus segmentation across imaging experiments: the 2018 data science bowl. *Nature Methods*, 16(12):1247–1253, 2019.

Laetitia Chapel, Mokhtar Z Alaya, and Gilles Gasso. Partial optimal transport with applications on positive-unlabeled learning. In *Advances in Neural Information Processing Systems*, volume 33, pages 2903–2913, 2020.

Hao Chen, Xiaojuan Qi, Lequan Yu, and Pheng-Ann Heng. Dcan: deep contour-aware networks for accurate gland segmentation. In *Proceedings of the IEEE/CVF Conference on Computer Vision and Pattern Recognition*, pages 2487–2496, 2016.

Richard J Chen, Tong Ding, Ming Y Lu, Drew FK Williamson, Guillaume Jaume, Andrew H Song, Bowen Chen, Andrew Zhang, Daniel Shao, Muhammad Shaban, et al. Towards a general-purpose foundation model for computational pathology. *Nature Medicine*, 30(3):850–862, 2024.

- Shengcong Chen, Changxing Ding, Minfeng Liu, Jun Cheng, and Dacheng Tao. Cpp-net: Context-aware polygon proposal network for nucleus segmentation. *IEEE Transactions on Image Processing*, 32:980–994, 2023a.
- Tianrun Chen, Lanyun Zhu, Chaotao Deng, Runlong Cao, Yan Wang, Shangzhan Zhang, Zejian Li, Lingyun Sun, Ying Zang, and Papa Mao. Sam-adapter: Adapting segment anything in underperformed scenes. In *Proceedings of the IEEE/CVF International Conference on Computer Vision*, pages 3367–3375, 2023b.
- Tianrun Chen, Ankang Lu, Lanyun Zhu, Chaotao Ding, Chunan Yu, Deyi Ji, Zejian Li, Lingyun Sun, Papa Mao, and Ying Zang. Sam2-adapter: Evaluating & adapting segment anything 2 in downstream tasks: Camouflage, shadow, medical image segmentation, and more. In *ICLR 2025 Workshop on Foundation Models in the Wild*, 2025a.
- Zhen Chen, Qing Xu, Xinyu Liu, and Yixuan Yuan. Un-sam: Domain-adaptive self-prompt segmentation for universal nuclei images. *Medical Image Analysis*, page 103607, 2025b.
- Zhiheng Cheng, Qingyue Wei, Hongru Zhu, Yan Wang, Liangqiong Qu, Wei Shao, and Yuyin Zhou. Unleashing the potential of sam for medical adaptation via hierarchical decoding. In *Proceedings of the IEEE/CVF Conference on Computer Vision and Pattern Recognition*, pages 3511–3522, 2024.
- Nicolas Courty, Rémi Flamary, Devis Tuia, and Alain Rakotomamonjy. Optimal transport for domain adaptation. *IEEE Transactions on Pattern Analysis and Machine Intelligence*, 39(9):1853–1865, 2016.
- Can Cui, Ruining Deng, Quan Liu, Tianyuan Yao, Shunxing Bao, Lucas W Remedios, Bennett A Landman, Yucheng Tang, and Yuankai Huo. All-in-sam: from weak annotation to pixel-wise nuclei segmentation with prompt-based finetuning. In *Journal of Physics: Conference Series*, 2024.
- Marco Cuturi. Sinkhorn distances: Lightspeed computation of optimal transport. In Advances in Neural Information Processing Systems, volume 26, 2013.
- Alexey Dosovitskiy, Lucas Beyer, Alexander Kolesnikov, Dirk Weissenborn, Xiaohua Zhai, Thomas Unterthiner, Mostafa Dehghani, Matthias Minderer, Georg Heigold, Sylvain Gelly, et al. An image is worth 16x16 words: Transformers for image recognition at scale. arXiv preprint arXiv:2010.11929, 2020.
- Jevgenij Gamper, Navid Alemi Koohbanani, Ksenija Benes, Simon Graham, Mostafa Jahanifar, Syed Ali Khurram, Ayesha Azam, Katherine Hewitt, and Nasir Rajpoot. Pannuke dataset extension, insights and baselines. arXiv preprint arXiv:2003.10778, 2020.
- Ruochen Gao, Donghang Lyu, and Marius Staring. Swin-litemedSAM: A lightweight box-based segment anything model for large-scale medical image datasets. In *Medical Image Segmentation Foundation Models. CVPR 2024 Challenge: Segment Anything in Medical Images on Laptop: MedSAM on Laptop*, 2024.
- Simon Graham, Quoc Dang Vu, Shan E Ahmed Raza, Ayesha Azam, Yee Wah Tsang, Jin Tae Kwak, and Nasir Rajpoot. Hover-net: Simultaneous segmentation and classification of nuclei in multi-tissue histology images. *Medical Image Analysis*, 58:101563, 2019.
- Noah F Greenwald, Geneva Miller, Erick Moen, Alex Kong, Adam Kagel, Thomas Dougherty, Christine Camacho Fullaway, Brianna J McIntosh, Ke Xuan Leow, Morgan Sarah Schwartz, et al. Whole-cell segmentation of tissue images with human-level performance using large-scale data annotation and deep learning. *Nature Biotechnology*, 40(4):555–565, 2022.
- Ishaan Gulrajani, Faruk Ahmed, Martin Arjovsky, Vincent Dumoulin, and Aaron C Courville. Improved training of wasserstein gans. In *Advances in Neural Information Processing Systems*, volume 30, 2017.
- Anubha Gupta, Shiv Gehlot, Shubham Goswami, Sachin Motwani, Ritu Gupta, Álvaro García Faura, Dejan Štepec, Tomaž Martinčič, Reza Azad, Dorit Merhof, et al. Segpc-2021: A challenge & dataset on segmentation of multiple myeloma plasma cells from microscopic images. *Medical Image Analysis*, 83:102677, 2023.
- Hongliang He, Zhongyi Huang, Yao Ding, Guoli Song, Lin Wang, Qian Ren, Pengxu Wei, Zhiqiang Gao, and Jie Chen. Cdnet: Centripetal direction network for nuclear instance segmentation. In *Proceedings of the IEEE/CVF International Conference on Computer Vision*, pages 4026–4035, 2021a.
- Hongliang He, Chi Zhang, Jie Chen, Ruizhe Geng, Luyang Chen, Yongsheng Liang, Yanchang Lu, Jihua Wu, and Yongjie Xu. A hybrid-attention nested unet for nuclear segmentation in histopathological images. Frontiers in Molecular Biosciences, 8:614174, 2021b.
- Hongliang He, Jun Wang, Pengxu Wei, Fan Xu, Xiangyang Ji, Chang Liu, and Jie Chen. Toposeg: Topology-aware nuclear instance segmentation. In *Proceedings of the IEEE/CVF International Conference on Computer Vision*, pages 21307–21316, 2023.

- Lina Huang, Yixiong Liang, and Jianfeng Liu. Des-sam: Distillation-enhanced semantic sam for cervical nuclear segmentation with box annotation. In *International Conference on Medical Image Computing and Computer-Assisted Intervention*, 2024a.
- Yuhao Huang, Xin Yang, Lian Liu, Han Zhou, Ao Chang, Xinrui Zhou, Rusi Chen, Junxuan Yu, Jiongquan Chen, Chaoyu Chen, Sijing Liu, Haozhe Chi, Xindi Hu, Kejuan Yue, Lei Li, Vicente Grau, Deng-Ping Fan, Fajin Dong, and Dong Ni. Segment anything model for medical images? *Medical Image Analysis*, 92:103061, 2024b. ISSN 1361-8415.
- Hao Jiang, Rushan Zhang, Yanning Zhou, Yumeng Wang, and Hao Chen. Donet: Deep de-overlapping network for cytology instance segmentation. In Proceedings of the IEEE/CVF Conference on Computer Vision and Pattern Recognition, pages 15641–15650, 2023.
- Qiangguo Jin, Hui Cui, Changming Sun, Jiangbin Zheng, Leyi Wei, Zhenyu Fang, Zhaopeng Meng, and Ran Su. Semi-supervised histological image segmentation via hierarchical consistency enforcement. In *International Conference on Medical Image Computing and Computer-Assisted Intervention*, pages 3–13, 2022.
- Sanghyun Jo, Seo Jin Lee, Seungwoo Lee, Seohyung Hong, Hyungseok Seo, and Kyungsu Kim. Coin: Confidence score-guided distillation for annotation-free cell segmentation. In *Proceedings of the IEEE/CVF International Conference on Computer Vision (ICCV)*, 2025.
- Leonid Kantorovich. On the transfer of masses (in russian). Doklady Akademii Nauk, 37:227, 1942.
- Alexander Kirillov, Eric Mintun, Nikhila Ravi, Hanzi Mao, Chloe Rolland, Laura Gustafson, Tete Xiao, Spencer Whitehead, Alexander C Berg, Wan-Yen Lo, et al. Segment anything. In *Proceedings of the IEEE/CVF International Conference on Computer Vision*, pages 4015–4026, 2023.
- Philip A. Knight. The sinkhorn–knopp algorithm: Convergence and applications. SIAM Journal on Matrix Analysis and Applications, 30(1):261–275, 2008.
- Neeraj Kumar, Ruchika Verma, Sanuj Sharma, Surabhi Bhargava, Abhishek Vahadane, and Amit Sethi. A dataset and a technique for generalized nuclear segmentation for computational pathology. *IEEE Transactions on Medical Imaging*, 36(7):1550–1560, 2017.
- C. Lanczos. Evaluation of noisy data. Journal of the Society for Industrial and Applied Mathematics Series B Numerical Analysis, 1(1):76–85, 1964.
- Chengyin Li, Rafi Ibn Sultan, Prashant Khanduri, Yao Qiang, Chetty Indrin, and Dongxiao Zhu. Autoprosam: Automated prompting sam for 3d multi-organ segmentation. In *Proceedings of the IEEE/CVF Winter Conference on Applications of Computer Vision*, pages 3570–3580, 2025.
- Feng Li, Hao Zhang, Huaizhe Xu, Shilong Liu, Lei Zhang, Lionel M Ni, and Heung-Yeung Shum. Mask dino: Towards a unified transformer-based framework for object detection and segmentation. In *Proceedings of the IEEE/CVF Conference on Computer Vision and Pattern Recognition*, pages 3041–3050, 2023.
- Yi Lin, Zhiyong Qu, Hao Chen, Zhongke Gao, Yuexiang Li, Lili Xia, Kai Ma, Yefeng Zheng, and Kwang-Ting Cheng. Nuclei segmentation with point annotations from pathology images via self-supervised learning and co-training. *Medical Image Analysis*, 89:102933, 2023.
- Weizhen Liu, Qian He, and Xuming He. Weakly supervised nuclei segmentation via instance learning. In *Proceedings* of the IEEE 19th International Symposium on Biomedical Imaging, pages 1–5, 2022.
- Xueyu Liu, Guangze Shi, Rui Wang, Yexin Lai, Jianan Zhang, Weixia Han, Min Lei, Ming Li, Xiaoshuang Zhou, Yongfei Wu, Chen Wang, and Wen Zheng. Segment any tissue: One-shot reference guided training-free automatic point prompting for medical image segmentation. *Medical Image Analysis*, 102:103550, 2025. ISSN 1361-8415.
- Yang Liu, Muzhi Zhu, Hengtao Li, Hao Chen, Xinlong Wang, and Chunhua Shen. Matcher: Segment anything with one shot using all-purpose feature matching. In *The Twelfth International Conference on Learning Representations*, 2024.
- Cheng Lu, David Romo-Bucheli, Xiangxue Wang, Andrew Janowczyk, Shridar Ganesan, Hannah Gilmore, David Rimm, and Anant Madabhushi. Nuclear shape and orientation features from h&e images predict survival in early-stage estrogen receptor-positive breast cancers. *Laboratory Investigation*, 98(11):1438–1448, 2018. ISSN 0023-6837.
- Yichuang Luo, Fang Wang, Jing Xing, and Xiaohu Liu. Groupprompter: A prompting method for semantic segmentation based on sam. *IEEE Access*, 11:106054–106062, 2023.

- Jun Ma, Yuting He, Feifei Li, Lin Han, Chenyu You, and Bo Wang. Segment anything in medical images. *Nature Communications*, 15(1):654, 2024.
- Anant Madabhushi and George Lee. Image analysis and machine learning in digital pathology: Challenges and opportunities. *Medical Image Analysis*, 33:170–175, 2016.
- Saiyang Na, Yuzhi Guo, Feng Jiang, Hehuan Ma, and Junzhou Huang. Segment any cell: A sam-based auto-prompting fine-tuning framework for nuclei segmentation. arXiv preprint arXiv:2401.13220, 2024.
- Peter Naylor, Marick Laé, Fabien Reyal, and Thomas Walter. Segmentation of nuclei in histopathology images by deep regression of the distance map. *IEEE Transactions on Medical Imaging*, 38(2):448–459, 2018.
- Kazuya Nishimura, Chenyang Wang, Kazuhide Watanabe, Dai Fei Elmer Ker, and Ryoma Bise. Weakly supervised cell instance segmentation under various conditions. *Medical Image Analysis*, 73:102182, 2021.
- Maxime Oquab, Timothée Darcet, Théo Moutakanni, Huy V. Vo, Marc Szafraniec, Vasil Khalidov, Pierre Fernandez, Daniel HAZIZA, Francisco Massa, Alaaeldin El-Nouby, Mido Assran, Nicolas Ballas, Wojciech Galuba, Russell Howes, Po-Yao Huang, Shang-Wen Li, Ishan Misra, Michael Rabbat, Vasu Sharma, Gabriel Synnaeve, Hu Xu, Herve Jegou, Julien Mairal, Patrick Labatut, Armand Joulin, and Piotr Bojanowski. DINOv2: Learning robust visual features without supervision. *Transactions on Machine Learning Research*, 2024. ISSN 2835-8856.
- Nobuyuki Otsu. A threshold selection method from gray-level histograms. *IEEE Transactions on Systems, Man, and Cybernetics*, 9(1):62–66, 1979.
- Marius Pachitariu and Carsen Stringer. Cellpose 2.0: how to train your own model. *Nature Methods*, 19(12):1634–1641, 2022.
- Zelin Peng, Zhengqin Xu, Zhilin Zeng, Xiaokang Yang, and Wei Shen. Sam-parser: Fine-tuning sam efficiently by parameter space reconstruction. In *Proceedings of the AAAI Conference on Artificial Intelligence*, pages 4515–4523, 2024.
- Hans Pinckaers, Wouter Bulten, Jeroen Van der Laak, and Geert Litjens. Detection of prostate cancer in wholeslide images through end-to-end training with image-level labels. *IEEE Transactions on Medical Imaging*, 40(7): 1817–1826, 2021.
- Hui Qu, Zhennan Yan, Gregory M Riedlinger, Subhajyoti De, and Dimitris N Metaxas. Improving nuclei/gland instance segmentation in histopathology images by full resolution neural network and spatial constrained loss. In *International Conference on Medical Image Computing and Computer-Assisted Intervention*, pages 378–386, 2019.
- Olaf Ronneberger, Philipp Fischer, and Thomas Brox. U-net: Convolutional networks for biomedical image segmentation. In *International Conference on Medical Image Computing and Computer-Assisted Intervention*, pages 234–241, 2015.
- Arnout C Ruifrok, Dennis A Johnston, et al. Quantification of histochemical staining by color deconvolution. *Analytical and Quantitative Cytology and Histology*, 23(4):291–299, 2001.
- Mihir Sahasrabudhe, Stergios Christodoulidis, Roberto Salgado, Stefan Michiels, Sherene Loi, Fabrice André, Nikos Paragios, and Maria Vakalopoulou. Self-supervised nuclei segmentation in histopathological images using attention. In *International Conference on Medical Image Computing and Computer-Assisted Intervention*, pages 393–402, 2020.
- Zhongyi Shui, Yunlong Zhang, Kai Yao, Chenglu Zhu, Sunyi Zheng, Jingxiong Li, Honglin Li, Yuxuan Sun, Ruizhe Guo, and Lin Yang. Unleashing the power of prompt-driven nucleus instance segmentation. In European Conference on Computer Vision, pages 288–304, 2024.
- Oriane Siméoni, Huy V Vo, Maximilian Seitzer, Federico Baldassarre, Maxime Oquab, Cijo Jose, Vasil Khalidov, Marc Szafraniec, Seungeun Yi, Michaël Ramamonjisoa, et al. Dinov3. arXiv preprint arXiv:2508.10104, 2025.
- Kai Sheng Tai, Peter D Bailis, and Gregory Valiant. Sinkhorn label allocation: Semi-supervised classification via annealed self-training. In *International Conference on Machine Learning*, pages 10065–10075, 2021.
- Kuan Tian, Jun Zhang, Haocheng Shen, Kezhou Yan, Pei Dong, Jianhua Yao, Shannon Che, Pifu Luo, and Xiao Han. Weakly-supervised nucleus segmentation based on point annotations: A coarse-to-fine self-stimulated learning strategy. In *International Conference on Medical Image Computing and Computer-Assisted Intervention*, pages 299–308, 2020.

- Abhishek Vahadane, Tingying Peng, Amit Sethi, Shadi Albarqouni, Lichao Wang, Maximilian Baust, Katja Steiger, Anna Melissa Schlitter, Irene Esposito, and Nassir Navab. Structure-preserving color normalization and sparse stain separation for histological images. *IEEE Transactions on Medical Imaging*, 35(8):1962–1971, 2016.
- Cédric Villani et al. Optimal transport: old and new, volume 338. Springer, 2008.
- Luc Vincent and Pierre Soille. Watersheds in digital spaces: an efficient algorithm based on immersion simulations. *IEEE Transactions on Pattern Analysis and Machine Intelligence*, 13(06):583–598, 1991.
- Eugene Vorontsov, Alican Bozkurt, Adam Casson, George Shaikovski, Michal Zelechowski, Kristen Severson, Eric Zimmermann, James Hall, Neil Tenenholtz, Nicolo Fusi, et al. A foundation model for clinical-grade computational pathology and rare cancers detection. *Nature Medicine*, 30(10):2924–2935, 2024.
- Quoc Dang Vu, Simon Graham, Tahsin Kurc, Minh Nguyen Nhat To, Muhammad Shaban, Talha Qaiser, Navid Alemi Koohbanani, Syed Ali Khurram, Jayashree Kalpathy-Cramer, Tianhao Zhao, et al. Methods for segmentation and classification of digital microscopy tissue images. Frontiers in Bioengineering and Biotechnology, 7:53, 2019.
- Jian Wang, Tianhong Dai, Bingfeng Zhang, Siyue Yu, Eng Gee Lim, and Jimin Xiao. Pot: Prototypical optimal transport for weakly supervised semantic segmentation. In *Proceedings of IEEE/CVF the Computer Vision and Pattern Recognition Conference*, pages 15055–15064, 2025.
- Xudong Wang, Rohit Girdhar, Stella X Yu, and Ishan Misra. Cut and learn for unsupervised object detection and instance segmentation. In Proceedings of the IEEE/CVF International Conference on Computer Vision and Pattern Recognition, pages 3124–3134, 2023.
- John N Weinstein, Eric A Collisson, Gordon B Mills, Kenna R Shaw, Brad A Ozenberger, Kyle Ellrott, Ilya Shmulevich, Chris Sander, and Joshua M Stuart. The cancer genome atlas pan-cancer analysis project. *Nature Genetics*, 45 (10):1113-1120, 2013.
- Huisi Wu, Zhaoze Wang, Youyi Song, Lin Yang, and Jing Qin. Cross-patch dense contrastive learning for semi-supervised segmentation of cellular nuclei in histopathologic images. In *Proceedings of the IEEE/CVF International Conference on Computer Vision*, pages 11656–11665, 2022.
- Junde Wu, Ziyue Wang, Mingxuan Hong, Wei Ji, Huazhu Fu, Yanwu Xu, Min Xu, and Yueming Jin. Medical sam adapter: Adapting segment anything model for medical image segmentation. *Medical Image Analysis*, 102:103547, 2025. ISSN 1361-8415.
- Qi Wu, Yuyao Zhang, and Marawan Elbatel. Self-prompting large vision models for few-shot medical image segmentation. In *Domain Adaptation and Representation Transfer: 5th MICCAI Workshop, DART 2023, Held in Conjunction with MICCAI 2023, Proceedings*, page 156–167, Berlin, Heidelberg, 2023. ISBN 978-3-031-45856-9.
- Enze Xie, Jiahao Lyu, Daiqing Wu, Huawen Shen, and Yu Zhou. Char-sam: Turning segment anything model into scene text segmentation annotator with character-level visual prompts. In *Proceedings of the IEEE International Conference on Acoustics, Speech and Signal Processing*, pages 1–5, 2025.
- Xinpeng Xie, Jiawei Chen, Yuexiang Li, Linlin Shen, Kai Ma, and Yefeng Zheng. Instance-aware self-supervised learning for nuclei segmentation. In *International Conference on Medical Image Computing and Computer-Assisted Intervention*, pages 341–350, 2020.
- Jie Xu, LiXiaokang, Chengyuyue, Chen Ma, Yi Guo, and Yuanyuan Wang. SAM-MPA: Applying SAM to few-shot medical image segmentation using mask propagation and auto-prompting. In Advancements In Medical Foundation Models: Explainability, Robustness, Security, and Beyond, 2024.
- Zhonghao Yan, Zijin Yin, Tianyu Lin, Xiangzhu Zeng, Kongming Liang, and Zhanyu Ma. Pgp-sam: Prototype-guided prompt learning for efficient few-shot medical image segmentation. In 2025 IEEE 22nd International Symposium on Biomedical Imaging, pages 1–5, 2025.
- Inwan Yoo, Donggeun Yoo, and Kyunghyun Paeng. Pseudoedgenet: Nuclei segmentation only with point annotations. In *International Conference on Medical Image Computing and Computer-Assisted Intervention*, pages 731–739, 2019.
- Chenyu You, Junlin Yang, Julius Chapiro, and James S Duncan. Unsupervised wasserstein distance guided domain adaptation for 3d multi-domain liver segmentation. *International Workshop on Interpretability of Machine Intelligence in Medical Image Computing*, pages 155–163, 2020.

- Chenyu You, Jinlin Xiang, Kun Su, Xiaoran Zhang, Siyuan Dong, John Onofrey, Lawrence Staib, and James S Duncan. Incremental learning meets transfer learning: Application to multi-site prostate mri segmentation. *International Workshop on Distributed, Collaborative, and Federated Learning*, pages 3–16, 2022a.
- Chenyu You, Ruihan Zhao, Fenglin Liu, Siyuan Dong, Sandeep Chinchali, Ufuk Topcu, Lawrence Staib, and James Duncan. Class-aware adversarial transformers for medical image segmentation. *Advances in neural information processing systems*, 35:29582–29596, 2022b.
- Chenyu You, Ruihan Zhao, Lawrence H Staib, and James S Duncan. Momentum contrastive voxel-wise representation learning for semi-supervised volumetric medical image segmentation. *International Conference on Medical Image Computing and Computer-Assisted Intervention*, pages 639–652, 2022c.
- Chenyu You, Yuan Zhou, Ruihan Zhao, Lawrence Staib, and James S Duncan. Simcvd: Simple contrastive voxel-wise representation distillation for semi-supervised medical image segmentation. *IEEE Transactions on Medical Imaging*, 41(9):2228–2237, 2022d.
- Chenyu You, Weicheng Dai, Yifei Min, Fenglin Liu, David Clifton, S Kevin Zhou, Lawrence Staib, and James Duncan. Rethinking semi-supervised medical image segmentation: A variance-reduction perspective. *Advances in neural information processing systems*, 36:9984–10021, 2023a.
- Chenyu You, Weicheng Dai, Yifei Min, Lawrence Staib, and James S Duncan. Bootstrapping semi-supervised medical image segmentation with anatomical-aware contrastive distillation. *International conference on information processing in medical imaging*, pages 641–653, 2023b.
- Chenyu You, Weicheng Dai, Yifei Min, Lawrence Staib, and James S Duncan. Implicit anatomical rendering for medical image segmentation with stochastic experts. *International Conference on Medical Image Computing and Computer-Assisted Intervention*, pages 561–571, 2023c.
- Chenyu You, Weicheng Dai, Yifei Min, Lawrence Staib, Jas Sekhon, and James S Duncan. Action++: Improving semi-supervised medical image segmentation with adaptive anatomical contrast. *International Conference on Medical Image Computing and Computer-Assisted Intervention*, pages 194–205, 2023d.
- Chenyu You, Weicheng Dai, Fenglin Liu, Yifei Min, Nicha C Dvornek, Xiaoxiao Li, David A Clifton, Lawrence Staib, and James S Duncan. Mine your own anatomy: Revisiting medical image segmentation with extremely limited labels. *IEEE Transactions on Pattern Analysis and Machine Intelligence*, 2024.
- Chenyu You, Haocheng Dai, Yifei Min, Jasjeet S Sekhon, Sarang Joshi, and James S Duncan. Uncovering memorization effect in the presence of spurious correlations. *Nature Communications*, 16(1):5424, 2025.
- Wenxi Yue, Jing Zhang, Kun Hu, Yong Xia, Jiebo Luo, and Zhiyong Wang. Surgicalsam: Efficient class promptable surgical instrument segmentation. In *Proceedings of the AAAI Conference on Artificial Intelligence*, 2024.
- Anqi Zhang, Guangyu Gao, Jianbo Jiao, Chi Harold Liu, and Yunchao Wei. Bridge the points: Graph-based few-shot segment anything semantically. In *Advances in Neural Information Processing Systems*, volume 37, pages 33232–33261, 2024a.
- Chuyu Zhang, Ruijie Xu, and Xuming He. Novel class discovery for long-tailed recognition. *Transactions on Machine Learning Research*, 2023. ISSN 2835-8856.
- Chuyu Zhang, Hui Ren, and Xuming He. P ² OT: Progressive partial optimal transport for deep imbalanced clustering. In *The Twelfth International Conference on Learning Representations*, 2024b.
- Renrui Zhang, Zhengkai Jiang, Ziyu Guo, Shilin Yan, Junting Pan, Hao Dong, Yu Qiao, Peng Gao, and Hongsheng Li. Personalize segment anything model with one shot. In *The Twelfth International Conference on Learning Representations*, 2024c.
- Tianyi Zhao and Zhaozheng Yin. Weakly supervised cell segmentation by point annotation. *IEEE Transactions on Medical Imaging*, 40(10):2736–2747, 2020.
- Xiuqi Zheng, Yuhang Zhang, Haoran Zhang, Hongrui Liang, Xueqi Bao, Zhuqing Jiang, and Qicheng Lao. Curriculum Prompting Foundation Models for Medical Image Segmentation . In *International Conference on Medical Image Computing and Computer-Assisted Intervention*, 2024.
- Yanning Zhou, Hao Chen, Huangjing Lin, and Pheng-Ann Heng. Deep semi-supervised knowledge distillation for overlapping cervical cell instance segmentation. In *International Conference on Medical Image Computing and Computer-Assisted Intervention*, pages 521–531, 2020.

Eric Zimmermann, Eugene Vorontsov, Julian Viret, Adam Casson, Michal Zelechowski, George Shaikovski, Neil Tenenholtz, James Hall, David Klimstra, Razik Yousfi, et al. Virchow2: Scaling self-supervised mixed magnification models in pathology. arXiv preprint arXiv:2408.00738, 2024.

Table of Contents

\mathbf{A}	The	eoretical Analysis	18
	A.1	Background	19
	A.2	Scaling Algorithm for Optimal Transport	19
	A.3	Derivation from Standard OT to Partial OT	20
	A.4	Proof of Equivalence with Partial OT	21
	A.5	Solver for Partial OT	22
В	Add	litional Implementation Details	23
	B.1	Datasets	23
	B.2	Metrics	24
	B.3	Implementation	24
	B.4	Illustrative Visualization	25
	B.5	Runtime Analysis	25
	B.6	Baselines	26
	B.7	Feature Extraction Backbones	27
	B.8	Additional Algorithms	29
\mathbf{C}	Add	litional Qualitative Results	30
	C.1	Segmentation Results across Datasets	30
	C.2	Comparison with Natural Image Segmentation Models	30
D	\mathbf{Adc}	litional Ablation Study	33
	D.1	Backbone Variants	33
	D.2	Feature Extractors across Datasets	33
	D.3	Point Quality and Generation	37
	D.4	Soft NMS	37
\mathbf{E}	\mathbf{Add}	litional Sensitivity Analysis	39
	E.1	SAM Effect	39
\mathbf{F}	Disc	cussion and Future Directions	39
	F.1	Beyond H&E	39

A Theoretical Analysis

In this section, we provide the theoretical foundations and complete proofs for Section 3.2. We begin with a brief discussion of applications of optimal transport (OT) to set the stage (Section A.1), followed by a review of its standard formulation and the entropic scaling algorithm for efficient computation (Section A.2). We then derive the partial OT formulation adopted in the POT-Scan module by extending from unbalanced OT in Section A.3. In particular, we show that introducing a slack column transforms partial OT into an equivalent unbalanced OT problem, which can be efficiently solved using Sinkhorn-based methods (Section A.4). Finally, we present the algorithm employed to solve partial OT in Section A.5.

A.1 Background

Optimal Transport (OT) (Villani et al., 2008) provides a mathematical framework for aligning one probability measure with another by finding the most cost-efficient way to reallocate mass. Classical OT corresponds to the case where exact mass preservation is enforced. Variants such as unbalanced OT relax the constraint to handle discrepancies in total mass. Adding entropic regularization (Zhang et al., 2023; Cuturi, 2013) to the objective function enables efficient approximation via Sinkhorn iterations, making large-scale applications practical. Beyond its theoretical elegance, OT has become a versatile tool in modern machine learning. It has supported advances in generative modeling by providing stable training objectives through Wasserstein distances (Gulrajani et al.,

```
Algorithm 1 Generalized scaling algorithm
```

```
1: Input: Cost C, regularization \epsilon > 0, marginals \mu \in \mathbb{R}_+^N, \nu \in \mathbb{R}_+^M

2: Q \leftarrow \exp(-C/\epsilon) \quad \triangleright \quad Q_{ij} = e^{-C_{ij}/\epsilon}

3: b \leftarrow \mathbf{1}_n

4: while not converged do

5: x \leftarrow Qb

6: \tilde{a} \leftarrow \operatorname{prox}_{\phi/\epsilon}^{KL}(x;\mu)

7: a \leftarrow \tilde{a} \oslash x \quad \triangleright \quad \text{elementwise division}

8: y \leftarrow Q^\top a

9: \tilde{b} \leftarrow \operatorname{prox}_{\psi/\epsilon}^{KL}(y;\nu)

10: b \leftarrow \tilde{b} \oslash y

11: end while

12: return T^* = \operatorname{diag}(a) Q \operatorname{diag}(b)
```

2017), in semi-supervised learning by enabling label propagation as a transport problem (Tai et al., 2021), and in domain adaptation by aligning feature distributions across domains (Courty et al., 2016).

A.2 Scaling Algorithm for Optimal Transport

The optimal transport problem can be formulated as a minimization task over transport plans that determine the cost-optimal way to move mass between two probability measures. Given probability vectors $\mu \in \mathbb{R}^{N \times 1}$, $\nu \in \mathbb{R}^{M \times 1}$, along with a cost matrix $C \in \mathbb{R}^{N \times M}$ defined on joint space, the objective function is written as:

$$\min_{T \in \mathbb{R}^{N \times M}} \langle T, C \rangle_F + \phi(T \mathbf{1}_M, \mu) + \psi(T^{\mathsf{T}} \mathbf{1}_N, \nu)$$
 (5)

where $T \in \mathbb{R}^{N \times M}$ denotes the transportation plan, $\langle \cdot \ , \cdot \rangle_F$ is the Frobenius product. ϕ and ψ are convex marginal distribution constraints, $\mathbf{1}_M \in \mathbb{R}^{M \times 1}$, $\mathbf{1}_N \in \mathbb{R}^{N \times 1}$ are all one vectors. This is the classical Kantorovich formulation (Kantorovich, 1942) if ϕ and ψ are equality constraints. By relaxing the marginal constraints via KL divergence or inequality penalties, the formulation allows controlled deviations from strict mass preservation. This leads to the unbalanced OT as described in Section A.3.

To make this problem computationally tractable, Cuturi (Cuturi, 2013) proposed entropic regularization. Adding the entropy term $-\epsilon \mathcal{H}(T)$ to objective function leads to the following formulation:

$$\langle T, C \rangle_F - \epsilon \mathcal{H}(T) = \epsilon \langle T, C/\epsilon + \log T \rangle_F = \epsilon \langle T, \log \frac{T}{\exp(-C/\epsilon)} \rangle_F = \epsilon K L(T || \exp(-C/\epsilon)), \tag{6}$$

Furthermore, Eq.(6) can be reformulated as:

$$\min_{T \in \mathbb{R}_{+}^{N \times M}} \epsilon KL\left(T || \exp(-C/\epsilon)\right) + \phi(T\mathbf{1}_{M}, \mu) + \psi(T^{\top}\mathbf{1}_{N}, \nu)\right). \tag{7}$$

Define the proximal operator as:

$$\operatorname{prox}_{f/\epsilon}^{KL}(y;z) = \arg\min_{x \ge 0} f(x,z) + \epsilon KL(x||y), \tag{8}$$

where z is the fixed parameter of the function f. In our case, z corresponds to the marginal distributions while f represents the associated marginal constraints ϕ or ψ . Then Eq.(7) can be solved approximately using Alg.(1).

These updates can be interpreted as Bregman projections with respect to the KL divergence onto convex sets defined by the marginal constraints (Benamou et al., 2015). Alternating such projections is guaranteed to converge, and the diagonal scaling form makes each iteration linear in the number of nonzero entries of Q. The entropic regularization enforces strict positivity, prevents sparsity and collapse of the transport plan, and

enhances numerical stability. Intuitively, the scaling vectors a, b can be viewed as per-row and per-column adjustment factors, respectively. Multiplying by a rescales entire rows to match μ , while multiplying by b rescales columns to align with ν . The iteratively alternating drives the transport plan T to satisfy the marginal structure.

As a result, whenever an optimal transport problem can be reformulated with suitable marginal constraints into the form of Eq.(5), the corresponding proximal operators can be derived as in Eq.(8). This allows the problem to be efficiently solved using Alg.(1).

A.3 Derivation from Standard OT to Partial OT

When strict equality constraints are not enforced, one may allow mass to be created or discarded. This leads to the unbalanced OT formulation where deviations from the marginals are penalized by a KL divergence. Assuming a uniform source distribution, Eq. (5) can be expressed as:

$$\min_{T \in \Pi} \langle T, C \rangle_F + \lambda K L(T^\top \mathbf{1}_N || \frac{1}{M} \mathbf{1}_M)$$
s.t.
$$\Pi = \{ T \in \mathbb{R}_+^{N \times M} || T \mathbf{1}_M = \frac{1}{N} \mathbf{1}_N \},$$
(9)

where λ is the regularization weight factor. Here, the row sums are fixed to the uniform source distribution, while the column sums are softly penalized toward uniformity.

Although unbalanced OT relaxes the marginal constraints, it still penalizes discrepancies between the transported and target mass. As a result, even ambiguous or noisy features are still encouraged to be moved, potentially degrading the quality of the solution. To address this limitation, we adopt the partial OT formulation, which explicitly controls the amount of total transported mass. Instead of hard-thresholding unreliable features, partial OT allows the model to reweigh and selectively transport a subset of the source samples by solving:

$$\min_{T \in \Pi} \langle T, C \rangle_F + \lambda K L(T^\top \mathbf{1}_N || \frac{\rho}{M} \mathbf{1}_M)$$
s.t. $\Pi = \{ T \in \mathbb{R}_+^{N \times M} | T \mathbf{1}_M \le \frac{1}{N} \mathbf{1}_N, \ \mathbf{1}_N^\top T \mathbf{1}_M = \rho \},$ (10)

where $N = h \times w$ is the uniform source feature and M = 2K is the number of target prototypes as described in Eq.(4). ρ specifies the total transported mass and will increase gradually. Intuitively, partial OT still respects the distributional structure but enables progressive selection of reliable samples. Low-cost correspondences are favored first, while noisier or ambiguous features can be safely ignored or deferred until ρ increases. This mechanism provides a principled way to suppress noise while guiding the optimization toward a globally consistent transport plan.

Mathematically, we follow prior work (Caffarelli and McCann, 2010; Chapel et al., 2020; Zhang et al., 2024b) to reformulate the partial OT problem as an unbalanced OT problem that can be solved efficiently with scaling algorithms. The key idea is to introduce a slack column into the marginal distribution to absorb the unselected mass $1 - \rho$, thereby turning the global mass constraint into a marginal one. Specifically, the slack column is denoted as $\eta \in \mathbb{R}^{N \times 1}$ to absorb the remaining mass and form the extended coupling:

$$\hat{T} = [T, \eta] \in \mathbb{R}^{N \times (M+1)}, \quad \hat{C} = [C, \mathbf{0}_N].$$

Imposing row-sum equality to the uniform source and total-mass accounting, we get:

$$\hat{T}\mathbf{1}_{M+1} = \frac{1}{N}\mathbf{1}_N, \quad \mathbf{1}_N^\top \eta = 1 - \rho, \quad \mathbf{1}_N^\top T \mathbf{1}_M = \rho.$$

Thus,

$$\hat{T}^{\top} \mathbf{1}_{N} = \begin{bmatrix} T^{\top} \mathbf{1}_{N} \\ \eta^{\top} \mathbf{1}_{N} \end{bmatrix} = \begin{bmatrix} T^{\top} \mathbf{1}_{N} \\ 1 - \rho \end{bmatrix}.$$
 (11)

Let the target column-mass prior be:

$$\beta = \left[\begin{array}{c} \frac{\rho}{M} \mathbf{1}_M \\ 1 - \rho \end{array} \right],$$

we can get the KL-penalized unbalanced surrogate of partial OT as follows:

$$\min_{\hat{T} \in \Phi} \langle \hat{T}, \hat{C} \rangle_F + \lambda K L(\hat{T}^\top \mathbf{1}_N || \boldsymbol{\beta})$$
s.t.
$$\Phi = \{ \hat{T} \in \mathbb{R}_+^{N \times (M+1)} | \hat{T} \mathbf{1}_{M+1} = \frac{1}{N} \mathbf{1}_N \}.$$
(12)

However, the KL term is soft. Eq.(12) does not guarantee the mass of the last column to be strictly $1 - \rho$. To recover the exact partial-OT constraint, a weighted KL constraint is employed to control the constraint strength for each class:

$$\hat{KL}(\hat{T}^{\top}\mathbf{1}_N||\beta;\hat{\lambda}) = \sum_{i=1}^{M+1} \lambda_i [\hat{T}^{\top}\mathbf{1}_N]_i \log \frac{[\hat{T}^{\top}\mathbf{1}_N]_i}{\beta_i},$$

with

$$\hat{\lambda} = \left[\begin{array}{c} \lambda \mathbf{1}_M \\ +\infty \end{array} \right].$$

This yields the final equivalent formulation:

$$\min_{T \in \Phi} \langle \hat{T}, \hat{C} \rangle_F + \hat{KL}(\hat{T}^{\top} \mathbf{1}_N || \beta; \hat{\lambda})$$
s.t.
$$\Phi = \{ \hat{T} \in \mathbb{R}_+^{N \times (M+1)} | \hat{T} \mathbf{1}_{M+1} = \frac{1}{N} \mathbf{1}_N \}.$$
(13)

The weighted KL makes the slack mass non-negotiable while keeping the real columns softly regularized. So low-cost correspondences are selected first, and ambiguous features can be safely left in the slack. The extended optimal plan is consistent with the original one, and the first M columns of the extended solution align with the optimal plan of the partial OT problem. The proof is provided in the next section.

A.4 Proof of Equivalence with Partial OT

In this section, we present the full proof that \tilde{T}^* , which is the first M columns of the extended optimal transport plan \hat{T}^* , corresponds exactly to the optimal plan T^* of the partial OT problem.

Proof. Assume the optimal extended plan is:

$$\hat{T}^{\star} = [\tilde{T}^{\star}, \eta^{\star}] \in \mathbb{R}^{N \times (M+1)}, \tilde{T}^{\star} \in \mathbb{R}^{N \times M}.$$

The weighted KL penalty expands as:

$$\begin{split} \hat{KL}(\hat{T}^{\star\top}\mathbf{1}_N||\boldsymbol{\beta};\hat{\boldsymbol{\lambda}}) &= \sum_{i=1}^{M} \lambda_i [\tilde{T}^{\star\top}\mathbf{1}_N]_i \log \frac{[\tilde{T}^{\star\top}\mathbf{1}_N]_i}{\beta_i} + \lambda_{M+1} \boldsymbol{\eta}^{\star\top}\mathbf{1}_N \log \frac{\boldsymbol{\eta}^{\star\top}\mathbf{1}_N}{1-\rho} \\ &= \lambda KL(\tilde{T}^{\star\top}\mathbf{1}_N||\frac{\rho}{M}\mathbf{1}_M) + \lambda_{M+1} \boldsymbol{\eta}^{\star\top}\mathbf{1}_N \log \frac{\boldsymbol{\eta}^{\star\top}\mathbf{1}_N}{1-\rho}. \end{split}$$

Taking the limit $\lambda_{M+1} \to +\infty$ forces the slack column to satisfy $\eta^{\star \top} \mathbf{1}_N = 1 - \rho$, otherwise the objective would diverge.

By construction, the extended plan satisfies the row constraint

$$\hat{T}^{\star} \mathbf{1}_{M+1} = \frac{1}{N} \mathbf{1}_N.$$

This can be written as

$$\tilde{T}^{\star} \mathbf{1}_M + \eta^{\star} = \frac{1}{N} \mathbf{1}_N, \eta^{\star} > 0,$$

we obtain

$$\tilde{T}^{\star}\mathbf{1}_{M}\leq \frac{1}{N}\mathbf{1}_{N}.$$

In addition, the total transported mass of the first M column is

$$\mathbf{1}_N^{\top} \tilde{T}^{\star} \mathbf{1}_M = \mathbf{1}_N^{\top} \hat{T}^{\star} \mathbf{1}_M - \mathbf{1}_N^{\top} \eta^{\star} = 1 - (1 - \rho) = \rho.$$

Therefore,

$$\tilde{T}^{\star} \in \{\tilde{T}^{\star} \in \mathbb{R}^{N \times M} | \tilde{T}^{\star} \mathbf{1}_{M} \leq \frac{1}{N} \mathbf{1}_{N}, \mathbf{1}_{N}^{\top} \tilde{T}^{\star} \mathbf{1}_{M} = \rho \},$$

which is precisely the feasible set of the partial OT problem.

Lastly, the cost of the extended problem is:

$$\langle \hat{T}^{\star}, \hat{C} \rangle_{F} + \hat{KL}(\hat{T}^{\star \top} \mathbf{1}_{N} || \boldsymbol{\beta}; \hat{\lambda}) = \langle [\tilde{T}^{\star}, \eta^{\star}], [C, \mathbf{0}_{n}] \rangle_{F} + \lambda KL(\tilde{T}^{\star \top} \mathbf{1}_{N}, \frac{\rho}{M} \mathbf{1}_{M})$$

$$= \langle \tilde{T}^{\star}, C \rangle_{F} + \lambda KL(\tilde{T}^{\star \top} \mathbf{1}_{N}, \frac{\rho}{M} \mathbf{1}_{M})$$
(14)

This is exactly the objective of the partial OT problem as in Eq.(10) evaluated at \tilde{T}^{\star} .

If \tilde{T}^* achieves a lower cost than T^* for the initial partial OT formula, it contradicts the optimality of T^* .

If T^* had strictly lower cost for Eq.(14), then \tilde{T}^* would no longer achieve the optimum, which would contradict the optimality of T^* .

As a result, by convexity of the objective, $\tilde{T}^{\star} = T^{\star}$. Dropping the last column of \hat{T}^{\star} , we achieve the optimal transport plan for the partial OT problem.

Solver for Partial OT **A.5**

Adding an entropy regularization term $-\epsilon \mathcal{H}(\hat{T})$ to Eq.(13) also enables the efficient scaling algorithm. We denote:

$$Q = \exp(-C/\epsilon), f = \frac{\lambda}{\lambda + \epsilon}, \alpha = \frac{1}{N} \mathbf{1}_N$$

The optimal plan admits the standard scaling form:

$$\hat{T}^* = \operatorname{diag}(a) \, Q \operatorname{diag}(b).$$

Proof. As shown in Section A.2, the main step is to compute the proximal operators corresponding to the constraints ϕ and ψ . To this end, let us first restate the Eq.(13) in a more general form:

$$\min_{T \in \Phi} \epsilon K L(T \parallel \exp(-C/\epsilon)) + \hat{KL}(T^{\top} \mathbf{1}_N || \beta; \lambda),
\text{s.t.} \quad \Phi = \{ T \in \mathbb{R}_{+}^{N \times M} \mid T \mathbf{1}_M = \alpha \}$$
(15)

Algorithm 2 Scaling algorithm for partial OT

- 1: Initialize: Cost matrix C, ϵ , λ , ρ , N, K, a large value ι
- 2: $C \leftarrow [C, \mathbf{0}_N],$
- 3: $\lambda \leftarrow [\lambda, ..., \lambda, \iota]^{\top}$ 4: $\beta \leftarrow [\frac{\rho}{M} \mathbf{1}_{M}^{\top}, 1 \rho]^{\top}$ 5: $\alpha \leftarrow \frac{1}{N} \mathbf{1}_{N}$
- 6: $b \leftarrow 1_{M+1}$
- 7: $Q \leftarrow \exp(-C/\epsilon)$ 8: $f \leftarrow \frac{\lambda}{\lambda + \epsilon}$
- 9: while b does not converge do
- 11:
- $a \leftarrow \frac{\alpha}{Mb} \\ b \leftarrow (\frac{\beta}{M^{+}a})^{\circ f}, \\ T \leftarrow \operatorname{diag}(a)Q\operatorname{diag}(b)$
- 13: end while
- 14: **return** T[:,:K]

where C is the cost matrix, α is the source marginal.

The equality constraint $T\mathbf{1}_M = \alpha$ can be expressed as the indicator:

$$\phi(x;\alpha) = \begin{cases} 0, & x = \alpha, \\ +\infty, & \text{otherwise.} \end{cases}$$

Plugging this into the proximal operator directly gives: $\operatorname{prox}_{\phi/\epsilon}^{KL}(y;\alpha) = \alpha$.

For the weighted KL penalty, the proximal operator is defined as:

$$\begin{aligned} \operatorname{prox}_{\psi/\epsilon}^{KL}(y;\beta) &= \arg\min_{x \ge 0} \ \hat{KL}(x||\beta;\lambda) + \epsilon \, KL(x||y) \\ &= \arg\min_{x \ge 0} \sum_{i=1}^{M+1} \lambda_i (x_i \log \frac{x_i}{\beta_i} - x_i + \beta) + \epsilon (x_i \log \frac{x_i}{y_i} - x_i + y_i). \end{aligned}$$

After dropping constants independent of x and regrouping terms, we obtain:

$$\operatorname{prox}_{\psi/\epsilon}^{KL}(y;\beta) = \arg\min_{x\geq 0} \sum_{i=1}^{M+1} (\lambda_i + \epsilon) x_i \log x_i - (\lambda_i \log \beta_i + \lambda_i + \epsilon \log y_i + \epsilon) x_i.$$

Consider the generic function $g(x) = ax \log x - bx$ with a > 0,

its derivative is $g'(x) = a(1 + \log x) - b$, hence the minimizer is $x^* = \exp(\frac{b-a}{a})$. Applying this result gives:

$$x_i^{\star} = \exp(\frac{\lambda_i \log \beta_i + \epsilon \log y_i}{\lambda_i + \epsilon}) = \beta_i^{\frac{\lambda_i}{\lambda_i + \epsilon}} y_i^{\frac{\epsilon}{\lambda_i + \epsilon}}.$$

In vector notation, we write:

$$x^* = \beta^{\circ f} \ y^{\circ (1-f)}, \quad f = \frac{\lambda}{\lambda + \epsilon},$$

where o denotes the element-wise power.

Now, substituting the two proximal operators into the general scaling algorithm yields the updates:

$$a \leftarrow \frac{\alpha}{Qb}, \quad b \leftarrow \left(\frac{\beta}{Q^{\top}a}\right)^{\circ f},$$

where $Q = \exp(-C/\epsilon)$.

The pseudo-code of the scaling algorithm for partial OT is provided in Alg.(2).

B Additional Implementation Details

B.1 Datasets

We conduct experiments on four challenging benchmark datasets of H&E stained histopathology images: MoNuSeg (Kumar et al., 2017), CPM17 (Vu et al., 2019), TNBC (Naylor et al., 2018), and PanNuke (Gamper et al., 2020).

- (I) MoNuSeg. MoNuSeg is a multi-organ nuclei segmentation dataset created from H&E-stained tissue images at 40× magnification from the TCGA archive (Weinstein et al., 2013), containing 51 images at 1000 × 1000 resolution from 7 organs with a total of 30,837 individually annotated nuclear boundaries. The MoNuSeg dataset contains 37 training images and 14 testing images.
- (II) CPM17. The CPM17 dataset contains 64 H&E stained histopathology images at 500×500 resolution with 7,670 annotated nuclei. Each image was scanned at $40 \times$ magnification. CPM17 includes 32 images each for training and testing.
- (III) TNBC. TNBC includes a collection of 50 H&E stained histopathology images of size 500×500 from Triple Negative Breast Cancer (TNBC) patients, containing 4,028 detailed nuclear annotations.
- (IV) PanNuke. The PanNuke dataset consists of 7,901 H&E-stained image patches, each sized 256×256 , spanning 19 different organs. In total, it provides 189,744 annotated nuclei. The dataset is partitioned into 2,656 training images, 2,523 validation images, and 2,722 testing images.

To facilitate patch-based processing for both feature extraction and SAM prediction, we use Lanczos interpolation (Lanczos, 1964) over 8×8 neighborhood to resize the MoNuSeg images to 1024×1024 , and the CPM17 and TNBC images to 512×512 . PanNuke images remain unchanged.

B.2 Metrics

Nuclear instance segmentation performance is evaluated using four instance-level metrics, including Detection Quality (DQ), Segmentation Quality (SQ), Panoptic Quality (PQ), and the Aggregated Jaccard Index (AJI), along with one semantic-level metric, the Dice coefficient (Dice). The detailed definitions are as follows:

Let $\mathcal{G} = \{G_i\}_{i=1}^{N_G}$ and $\mathcal{P} = \{P_j\}_{j=1}^{N_P}$ denote the sets of ground-truth and predicted instances, respectively. Define the IoU (Intersection over Union) as below:

$$IoU_{ij} = \frac{|G_i \cap P_j|}{|G_i \cup P_j|}.$$

Dice. Dice score measures overall pixel-level agreement and is insensitive to instance identities. It can be calculated using foreground overlap after binarization:

Dice =
$$\frac{2 \left| \left(\cup_i G_i \right) \bigcap \left(\cup_j P_j \right) \right|}{\left| \cup_i G_i \right| + \left| \cup_j P_j \right|}.$$

AJI (Aggregated Jaccard Index). AJI is an instance-aware Jaccard that penalizes both split and merged instances since the unmatched regions go to the denominator.

Let $\mathcal{M} \subseteq \{1, \ldots, N_G\} \times \{1, \ldots, N_P\}$ be a one-to-one matching between instances with $IoU_{ij} > 0$. Then, AJI can be calculated as:

$$AJI = \frac{\sum_{(i,j)\in\mathcal{M}} |G_i \cap P_j|}{\sum_{(i,j)\in\mathcal{M}} |G_i \cup P_j| + \sum_{i:(i,\cdot)\notin\mathcal{M}} |G_i| + \sum_{j:(\cdot,j)\notin\mathcal{M}} |P_j|}.$$

PQ, DQ, and SQ. Detection Quality (DQ) quantifies the accuracy of instance detection by accounting for false positives and false negatives, while Segmentation Quality (SQ) measures the delineation accuracy of correctly matched instances. Panoptic Quality (PQ), defined as the product of DQ and SQ, provides a comprehensive metric that jointly reflects both detection and segmentation performance.

The matched pairs (true positive) are defined with a fixed threshold $\tau = 0.5$.

$$TP = \{(i, j) : IoU_{ij} > \tau\}.$$

Let $FP = N_P - |TP|$ and $FN = N_G - |TP|$. Then

$$DQ = \frac{|TP|}{|TP| + \frac{1}{2}FP + \frac{1}{2}FN}, \quad SQ = \frac{1}{|TP|} \sum_{(i,j) \in TP} IoU_{ij},$$
$$PQ = DQ \times SQ.$$

In practice, the one-to-one correspondences between ground truth and predicted instances are established using a greedy matching strategy. The evaluation metrics are subsequently obtained by averaging results across all images.

B.3 Implementation

General Settings. Our method is training-free and therefore does not require dataset partitioning. To ensure a fair comparison with the trained networks, we conduct evaluations on the fixed test sets of MoNuSeg and CPM17. For TNBC, we randomly split the data with an 80/20 ratio for training and testing. The PanNuke dataset partition follows the predefined folds provided in its official release. All experiments are performed on a single NVIDIA GeForce RTX 4090 GPU with 24 GB of memory. Each experiment is repeated three times, and the average performance is reported.

Baseline Reproduction. For baseline model comparison, we use the official source code released by the authors on GitHub and follow the recommended configurations in the original publications. U-Net predictions are converted into instance segmentation masks using the watershed algorithm. For baselines that require

user input, prompts are generated from the ground truth when no automatic prompt generation mechanism is available. Note that we employ automatic grid-point prompting rather than ground-truth point prompts for the vanilla SAM model. All reported numbers correspond to our reproduced results.

Sensitivity Studies. Sensitivity studies are conducted on the MoNuSeg dataset using a patch size of 128×128 and a stride of 64 for feature extraction with Virchow2. Default settings are as follows: the initial high-confidence mask ratio is 0.6 (varied in Figure 11a), the number of prototype centers is 3 (changed in Figure 11d), the initial OT weight is 0.6 (investigated in Figure 11b), and the POT-Scan weight stride is 0.05 (analyzed in Figure 11c). The large SAM weights are employed, and images are tiled into 512×512 patches with an overlap ratio of 0.5 (tuned in Figure 11f). For prediction, each positive point and two negative points are provided to SAM (altered in Figure 11e). Containment-aware soft NMS is applied in the post-processing stage.

B.4 Illustrative Visualization

To provide a conceptual understanding of stain priors as discussed in Section 3.1, we illustrate in Figure 12 how hematoxylin and eosin channels naturally separate nuclei from surrounding tissue, producing two complementary intensity maps that act as reliable cues for locating foreground and background regions. This inherent contrast structure allows us to obtain location priors directly from the image without any manual annotations. By overlapping the high-confidence masks derived from the strongest optical density responses with the encoded feature map, we focus on the most concrete and representative nuclear and non-nuclear areas for the following prototype construction. This vields clean and reliable reference features that anchor downstream clustering and similarity mapping rather than arbitrary or heuristic choices.

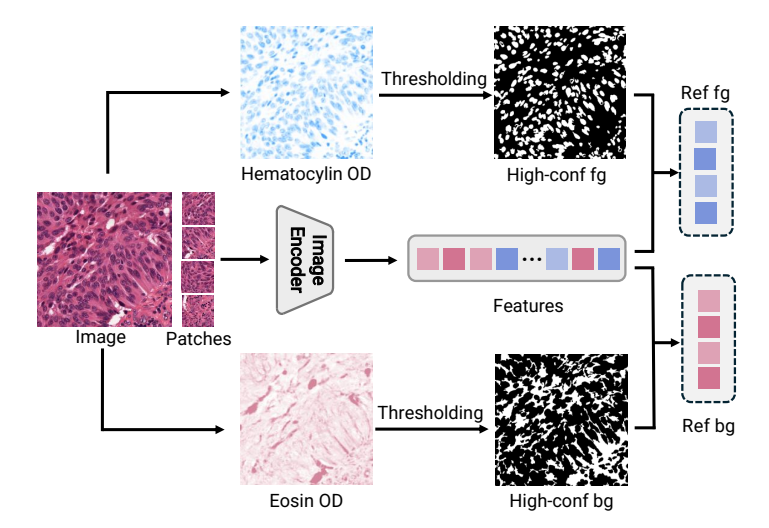


Figure 12 Visualization of stain prior guided features extraction for self-reference. Hematoxylin and eosin intensity maps from optical density decomposition are thresholded to produce high-confidence foreground and background masks, which are applied to the encoded feature map to extract reference features for subsequent prototype construction.

B.5 Runtime Analysis

To fully assess the computational overhead of our approach in practical settings as a complement to Figure 6 in Section 4.2, we report detailed runtime statistics for the point-generation pipeline. The runtime breakdown for each step in the point-generation pipeline is summarized in Table 2a and 2b. The initial mask stage, which identifies coarse foreground and background regions from stain information, is required for all methods. The prototype stage performs feature extraction and K-means clustering to construct reference prototypes. Greedy search assigns features directly to their nearest prototypes and serves as a baseline against OT.

Otsu's method uses solely the stain-intensity histogram of the input image, operating on optical-density values without any feature encoding, clustering, or contextual reasoning. This simplified thresholding is fast but yields coarse separation of nuclear and non-nuclear regions. Greedy assignment provides a stronger baseline by performing a local nearest-prototype lookup for each feature vector. It has a computational complexity of O(NK), where N is the number of feature vectors and K is the number of prototypes. This operation is essentially a single cosine-similarity pass over the encoded feature map. As a result, it is fast but remains inherently local, lacking any global consistency constraint. In contrast, Optimal Transport methods solve a global alignment problem using Sinkhorn iterations, typically requiring O(T(NK)) operations, where T is the number of iterations. POT-Scan reformulates partial OT into a series of balanced OT problems and

gradually increases the transported mass. Although this usually converges in 1–3 mass-increase steps per image, each step requires solving an OT problem. Consequently, it is slower than greedy matching or Otsu, but the runtime remains comparable to the feature-extraction stage, the dominant cost across methods.

Critically, the additional computation of the POT-Scan module is not overhead for its own sake. The partial-mass formulation enables POT to discard ambiguous, low-confidence features while focusing transport on the most reliable structures. This global, noise-aware selection mechanism yields stable and high-quality point prompts, particularly useful in challenging histopathology images where local heuristics often fail. In this context, the computational cost becomes an economically reasonable trade-off for obtaining globally consistent, noise-robust prototype alignment.

Additionally, both feature extraction and OT naturally scale with image resolution. The CPM17 datasets with smaller inputs (512×512) exhibit shorter runtime than the high-resolution MoNuSeg dataset, where images are 1024×1024 . Moreover, hyperparameters such as the initial mass and spatial stride offer practical trade-offs between runtime and accuracy. Increasing either parameter reduces computation while incurring only minor performance degradation since the method is insensitive to these hyperparameter settings.

Table 2 Point generation runtime breakdown on MoNuSeg and CPM17. Both tables report runtime in seconds without parallel processing. Feature extraction resolution: 128×128 . Partial OT initialized with weight 0.7 and stride 0.05.

(a) MoNuSeg. Image size: 1024×1024 .

<i>-</i>		т .	F10	F10
In	('P\/II'/	Image size:	\sim	っしい
\N.	OI WII .	IIIIage Size.	914 A	014.

Stage	Otsu	greedy	balanced	partial		Stage	Otsu	greedy	balanced	partial
Inital mask	0.359	0.341	0.341	0.341	-	Inital mask	0.076	0.071	0.071	0.071
Prototype	-	6.024	6.024	6.024		Prototype	-	0.963	0.963	0.963
Mapping	-	0.001	3.279	9.605		Mapping	-	0.001	0.618	1.991
Point-gen	0.137	0.137	0.137	0.137		Point-gen	0.027	0.027	0.027	0.027
End-to-end	0.488	6.503	9.781	16.107		End-to-end	0.103	1.062	1.679	3.052

B.6 Baselines

We provide detailed descriptions of the baseline models used for comparison in Section 4.1. Their implementation settings and necessary adaptations are provided in Section B.3.

U-Net. U-Net (Ronneberger et al., 2015) is a classic convolutional neural network architecture for biomedical image segmentation. Its encoder–decoder design combines a contracting path for contextual extraction with an expansive path for precise localization through symmetric skip connections. This structure allows U-Net to learn fine-grained spatial details from limited training data, making it a widely adopted baseline for medical segmentation tasks.

SPN+IEN. SPN+IEN (Liu et al., 2022) is a weakly supervised framework that uses point annotations for nuclei segmentation. It separates the task into two complementary modules: a Semantic Proposal Network (SPN) that generates coarse foreground–background masks, and an Instance Encoding Network (IEN) that learns instance-aware pixel embeddings to distinguish neighboring nuclei. Such a design reduces annotation costs while maintaining strong segmentation performance.

SC-Net. Shape-Constrained Network (SC-Net) (Lin et al., 2023) integrates morphological shape priors into the learning process for nuclei instance segmentation. It employs a detection branch to localize nuclei and a segmentation branch to refine masks. Shape constraints are enforced to better handle overlapping or irregularly shaped nuclei.

Segment Anything Model. SAM (Kirillov et al., 2023) is a foundation segmentation model designed for interactive instance segmentation. It consists of an image encoder, a prompt encoder, and a lightweight mask decoder. By leveraging spatial or textual prompts (points, boxes, masks), SAM produces high-quality predictions in a zero-shot manner across diverse domains.

DES-SAM. DES-SAM (Huang et al., 2024a) is a distillation-enhanced adaptation of SAM for box-supervised nucleus segmentation. It incorporates a lightweight detection module to generate bounding-box

prompts and uses a self-distillation prompting strategy to leverage SAM's pretrained knowledge while fine-tuning a small number of parameters. DES-SAM introduces an edge-aware loss to refine boundary quality as well. Together, these components allow DES-SAM to achieve accurate segmentation with limited supervision while preserving SAM's strong generalization ability.

MedSAM. MedSAM (Ma et al., 2024) adapts the SAM to the medical domain and serves as a foundation model for universal medical image segmentation. It is trained on an unprecedented dataset of over 1.5 million image—mask pairs, spanning 10 imaging modalities and over 30 cancer types. In this way, it captures a wide spectrum of anatomical structures and pathological conditions. Like SAM, MedSAM is also a promptable segmentation system, where the user inputs bounding boxes to guide the delineation of regions of interest.

UN-SAM. UN-SAM (Chen et al., 2025b) introduces a domain-adaptive self-prompting framework for nuclei segmentation. To remove the manual annotations, it employs a self-prompt generation module to produce high-quality segmentation hints automatically. It further strengthens cross-domain generalization by combining shared representations with domain-specific adaptations, allowing robust performance on heterogeneous nuclei images.

Med-SA. Medical SAM Adapter (Med-SA) (Wu et al., 2025) extends SAM to medical imaging via parameter-efficient fine-tuning, updating only about 2% of its parameters. It introduces two key components: SD-Trans, which adapts SAM to 3D medical data, and the Hyper-Prompting Adapter (HyP-Adpt), which conditions the model on user-provided prompts for interactive segmentation. Med-SA supports both point clicks and bounding box prompts for prediction.

COIN. COIN (COnfidence score-guided INstance distillation) (Jo et al., 2025) is an annotation-free framework designed for unsupervised cell instance segmentation. Its three-step pipeline consists of feature extraction with pixel-level propagation, optimal transport—based refinement, SAM-driven instance-level consistency scoring, and recursive self-distillation. It identifies, evaluates, and reinforces reliable pseudo-labels to train a base segmentation network. Overall, COIN offers a simple yet effective strategy for producing high-quality supervisory signals without annotations, introducing a fully unsupervised instance-level confidence scoring paradigm for cell segmentation.

Both COIN and our method operate entirely without annotations. However, COIN begins with a weak initial model and relies on iterative training cycles to strengthen it through distilled supervision. In contrast, our method avoids the training stage altogether by leveraging stain-derived priors to directly obtain high-confidence references for point prompt generation, making it substantially more efficient and faster while preserving strong segmentation quality.

B.7 Feature Extraction Backbones

UNI, UNI2. UNI (Chen et al., 2024) is a pathology-specific vision encoder built with self-supervised pretraining on a large scale. More than 100 million image tiles drawn from around 100,000 diagnostic slides were used. It demonstrates strong transfer across a wide range of pathology tasks, particularly excelling in settings involving rare or underrepresented cancers. UNI-2 enlarges the pretraining corpus to over 200 million H&E and immunohistochemistry (IHC) images from more than 350,000 slides. By incorporating greater scale and modality diversity, UNI-2 further improves generalization across diagnostic tasks. It provides the community with an openly available resource for developing and benchmarking computational pathology models.

Virchow, Virchow2. The Virchow model family (Zimmermann et al., 2024; Vorontsov et al., 2024) represents an effort to establish foundation encoders tailored to digital pathology. Virchow was trained in a self-supervised manner on a vast collection of histopathology tiles obtained from millions of whole-slide images (WSIs). This large-scale pretraining equips the model with a broad awareness of tissue architecture and cellular morphology, which can then be transferred to downstream tasks such as cancer subtyping, outcome prediction, or biomarker discovery. Virchow2 extends this approach by further scaling the training corpus to more than 3.1 million WSIs, positioning it among the largest pathology encoders. Beyond its scale, Virchow2 can also serve as a frozen feature extractor for efficient pipeline integration or be fine-tuned to maximize performance on task-specific datasets.

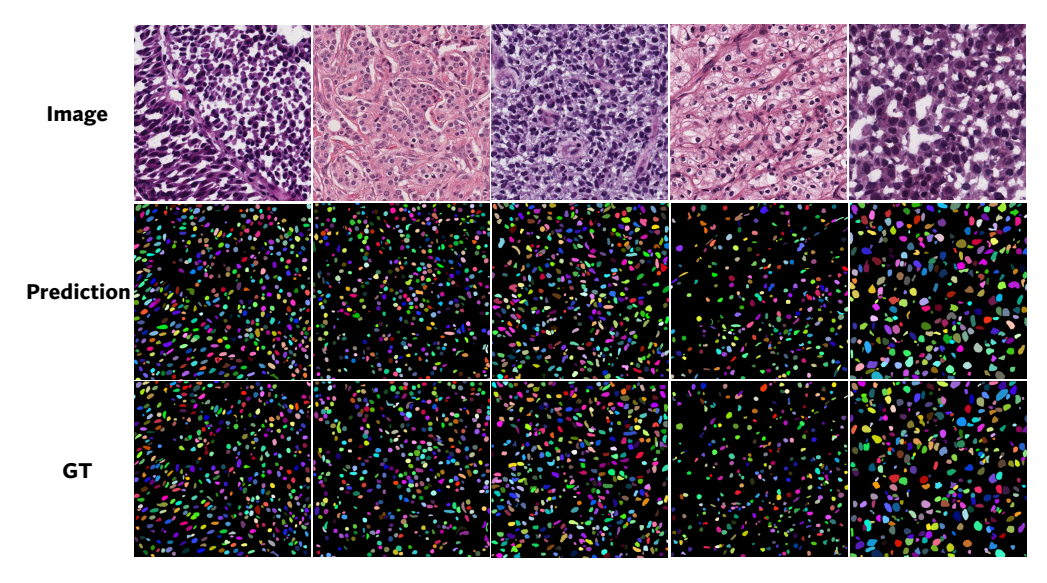


Figure 13 Visualization of segmentation results on MoNuSeg. Our method accurately distinguishes nuclear regions from surrounding white and stained tissues, and maintains robustness in dense and small nucleus scenarios. Each image may contain thousands of nuclei, and the SPROUT consistently identifies and segments them with high fidelity.

H-optimus-1. H-optimus-1 (Bioptimus, 2025) is a 1.1B-parameter vision transformer developed by Bioptimus. It was pretrained with self-supervised learning on billions of histology tiles from over one million slides. It produces rich patch embeddings that capture complex spatial and structural relationships, supporting downstream tasks such as survival analysis, tissue classification, and segmentation.

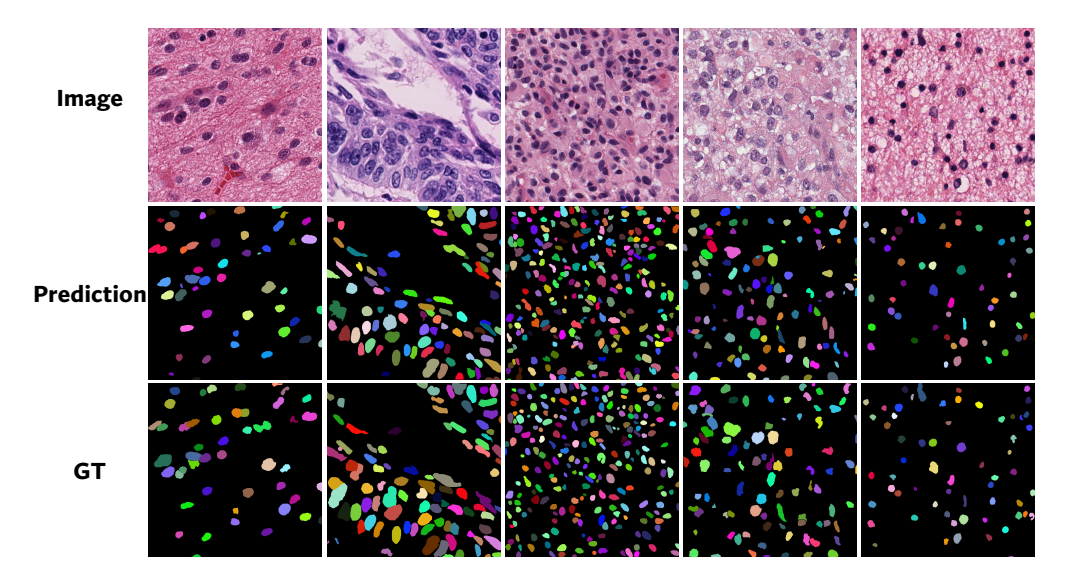


Figure 14 Visualization of segmentation results on CPM17. SPROUT effectively segments target nuclei in small-scale images when the input exhibits clear foreground–background separation, lightly separated nuclear regions, or tissue and nuclei with similar purple hues that make background discrimination challenging.

DINOv2, DINOv3. DINOv2 (Oquab et al., 2024) is a self-supervised vision transformer pretrained on a curated collection of 142 million images and is designed to produce general-purpose visual features comparable to those learned by weakly or fully supervised methods. Its representations transfer effectively across domains, enabling broad use without task-specific fine-tuning. DINOv3 (Siméoni et al., 2025) extends DINOv2 by scaling pretraining to over a billion images and models with billions of parameters. It further introduces mechanisms to stabilize training and preserve dense feature quality. With additional distillation into smaller, efficient variants, it achieves superior performance on both recognition and dense prediction

tasks, underscoring the role of scale-aware design in vision foundation models.

ViT-l/16. The Vision Transformer (ViT) family adapts the Transformer architecture to images by treating fixed-size patches as tokens. Among its configurations, ViT-l/16 (Large, 16×16 patch size) (Dosovitskiy et al., 2020) has become a widely adopted backbone due to its balance of scale and granularity. It consists of 24 Transformer layers with a hidden dimension of 1024 and roughly 307M parameters. Pretraining on large-scale datasets demonstrates that ViT-l/16 gains substantial improvements from scaling. Its 16×16 patch size ensures a manageable sequence length while preserving sufficient spatial resolution, making it a widely used backbone and a standard reference model for feature extraction in vision transformers.

B.8 Additional Algorithms

Watershed algorithm. The watershed algorithm (Vincent and Soille, 1991) is a classical segmentation approach for delineating touching or overlapping objects. It operates on the analogy of a topographic surface, where the grayscale image is interpreted as an elevation map. Pixels of lower intensity correspond to basins (valleys), whereas higher intensity values represent ridges (peaks). By flooding this landscape, water initially fills the basins, and as the level rises, neighboring catchment areas begin to merge. To prevent such mergers, separating boundaries are introduced at the points of convergence, thereby yielding distinct object regions. In practice, the algorithm is driven by the inverse of the distance transform, with local maxima serving as initial seeds or markers that guide the flooding process. Within our framework, the centroid of each resulting watershed region is used as the positive point prompt for prompt-based segmentation.

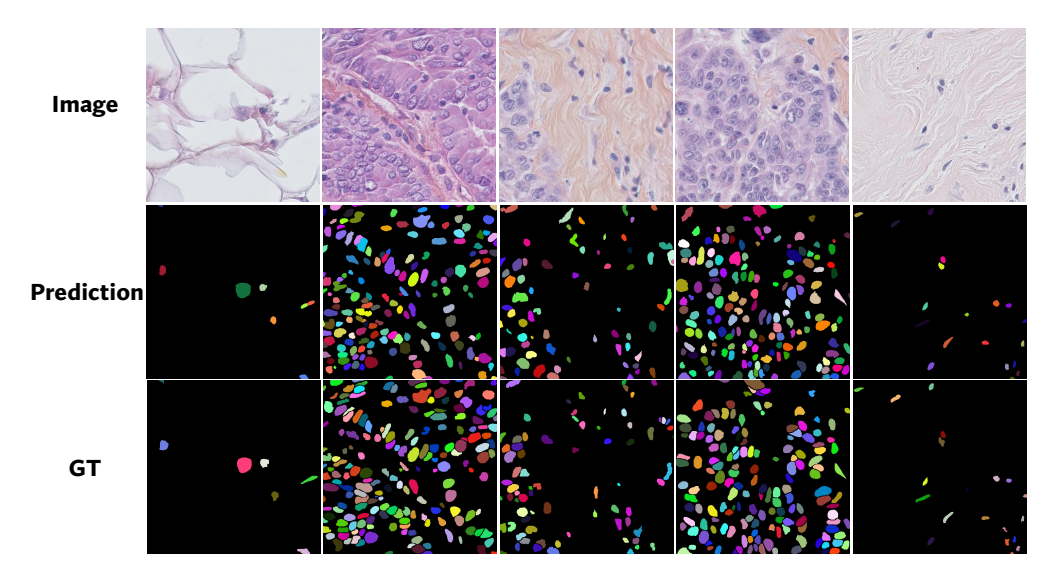


Figure 15 Visualization of segmentation results on TNBC. Our method remains effective on the TNBC dataset collected under different protocols with an additional transparency channel beyond standard RGB. It performs robustly in both sparse settings with only dozens of nuclei and highly crowded cases with hundreds, accurately distinguishing nuclear regions with minimal omission.

Otsu's thresholding. Otsu's thresholding (Otsu, 1979) is a global image binarization technique that selects the threshold t^* by minimizing the intra-class variance of foreground and background pixels, which is equivalent to maximizing the between-class variance.

Suppose the image histogram has L gray levels, with normalized probabilities p_i for each level i. For a given threshold t, the images are divided into two classes: class 0 with gray level $1, \dots, t$ with probability $w_0(t) = \sum_{i=1}^t p_i$ and mean $\theta_0(t)$, class 1 with gray level $t+1\cdots, L$ with probability $w_1(t) = \sum_{i=t+1}^L p_i$ and mean $\theta_1(t)$. The total mean is $\theta_T = \sum_{i=1}^L ip_i$. The between-class variance is:

$$\sigma^{2}(t) = w_{0}(t)(\theta_{0}(t) - \theta_{T})^{2} + w_{1}(t)(\theta_{1}(t) - \theta_{T})^{2}$$

Otsu's method chooses the threshold:

$$t^* = \arg\max_t \sigma^2(t),$$

which maximizes the separation between the two classes. This makes the method non-parametric and unsupervised, requiring no prior knowledge about the image content for foreground–background separation.

C Additional Qualitative Results

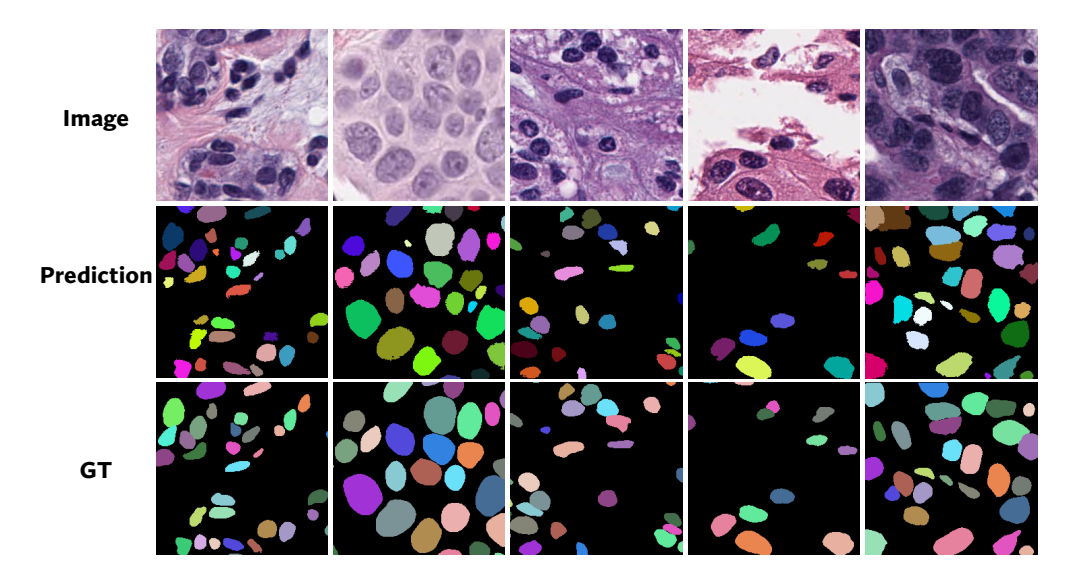


Figure 16 Visualization of segmentation results on PanNuke. PanNuke contains relatively larger and fewer nuclei with diverse tissue origins. These examples demonstrate the generalizability of our method across diverse nuclear morphologies and stain appearances, despite substantial structural and visual variation.

In this section, we provide the qualitative visualizations of segmentation results from our SPROUT pipeline across four datasets (Section C.1), complementing the analysis in Figure 4. For comparison, we also include results from semantic and instance segmentation models developed for natural images in Section C.2. It helps illustrate the gap between natural and pathological domains and highlights the unique challenges of nuclear image segmentation discussed in Introduction (Section 1).

C.1 Segmentation Results across Datasets

As illustrated in Figure 13-16, SPROUT delivers accurate nuclear segmentation across diverse datasets. The method demonstrates robustness under varying cellular organizations, from crowded fields containing thousands of nuclei (Figure 13 and Figure 14) to extremely sparse images with only a few (Figure 15). It performs well even when nuclei are small, densely packed, or exhibit subtle color contrasts with surrounding tissues. Moreover, SPROUT adapts seamlessly to the TNBC dataset, which is acquired with different staining protocols and image formats, including those with non-standard channels, consistently producing reliable delineations. It also generalizes robustly to the PanNuke dataset in Figure 16, where the relatively large spatial coverage of nuclei often risks over-segmentation. SPROUT preserves coherent nuclear structures without fragmenting any individual cells. Note that both predicted and ground-truth instance masks are displayed with randomly assigned colors, which serve only to differentiate instances for better visualization. Identical colors do not imply correspondence across cells or categories.

C.2 Comparison with Natural Image Segmentation Models

To assess the intrinsic difference between segmentation models developed for natural images and those tailored to pathological images, we apply annotation-free natural image models to nuclear segmentation. Specifically, we choose SAM (Kirillov et al., 2023), MaskDINO (Li et al., 2023), and CutLER (Wang et al., 2023) for instance segmentation and Bridge the Points (Zhang et al., 2024a) for one-shot semantic segmentation. The detailed description of SAM is provided in Appendix Section B.6, while the remaining models are summarized below. The corresponding segmentation results are also presented for comparison.

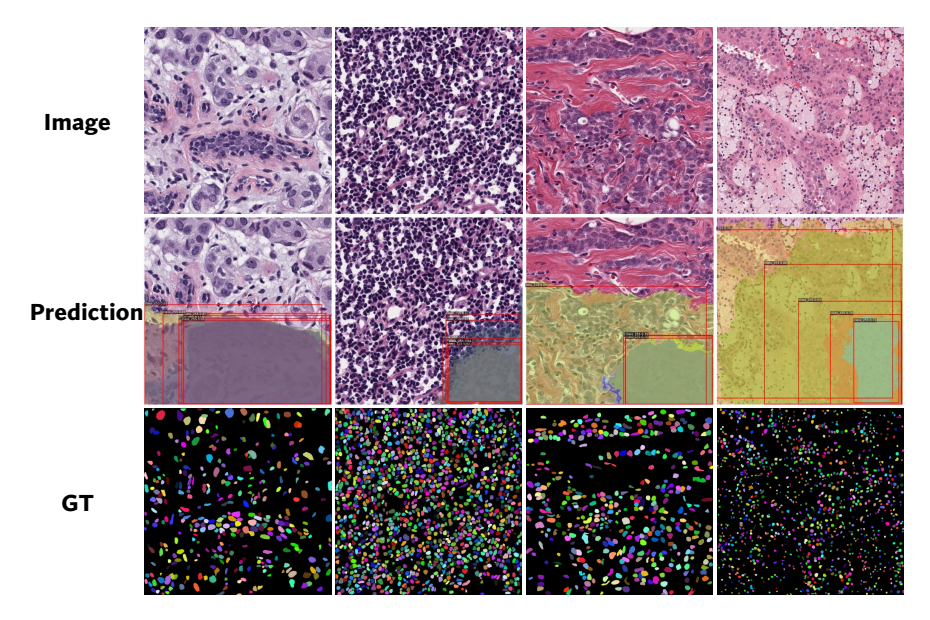


Figure 17 Visualization of segmentation results from Mask DINO. The model highlights broad tissue regions but fails to resolve individual nuclei.

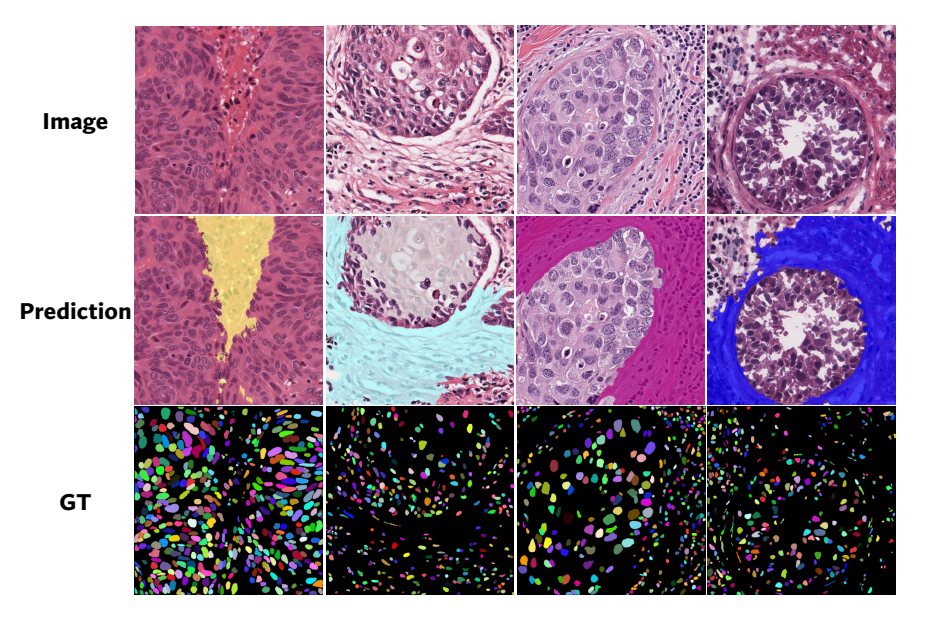


Figure 18 Visualization of segmentation results from CutLER. The model segments coarse regions with boundary changes but fails to capture fine-grained nuclear structures. The colored areas denote the produced masks.

SAM. As shown in Figure 19, SAM auto-prompting operates on a fixed 32×32 grid, which fails to distinguish foreground from background reliably and cannot ensure coverage of all nuclei. Large tissue regions are often misclassified as targets, which suppresses small-cell predictions either due to lower SAM scores or the lack of point prompts generated on a coarse grid. In addition, because the selection of final masks relies on morphological scores rather than semantic information or negative prompts, the resulting masks frequently exhibit over-segmentation, reflecting SAM's dependence on purely visual cues and the strong similarity between nuclear regions and surrounding background textures.

Mask DINO. Mask DINO extends the transformer-based object detector DINO by adding a parallel mask prediction branch, thereby unifying detection with instance, semantic, and panoptic segmentation through shared query embeddings for bounding box regression and mask generation. Pretrained on large-scale detection and segmentation datasets, it achieves strong performance on natural image benchmarks.

However, as shown in Figure 17, its performance on MoNuSeg is limited. The top predictions frequently overlap on large tissue regions rather than capturing individual nuclei. This behavior suggests a tendency to segment regions of homogeneous texture or color areas, while failing to delineate fine-grained nuclear structures.

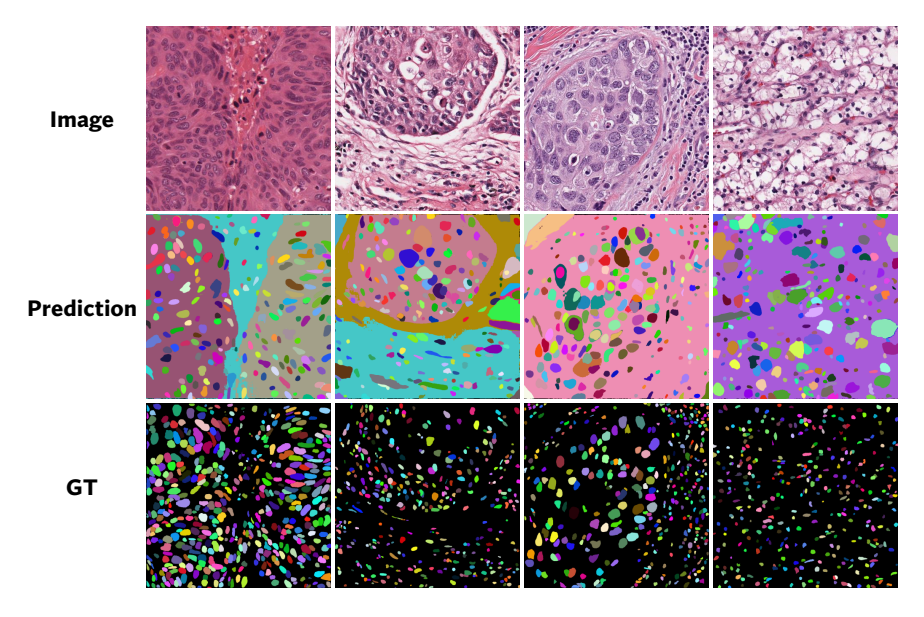


Figure 19 Visualization of instance segmentation results from SAM auto-prompting. SAM captures a subset of nuclei but struggles to separate nuclei from background tissues, leading to compromised segmentation.

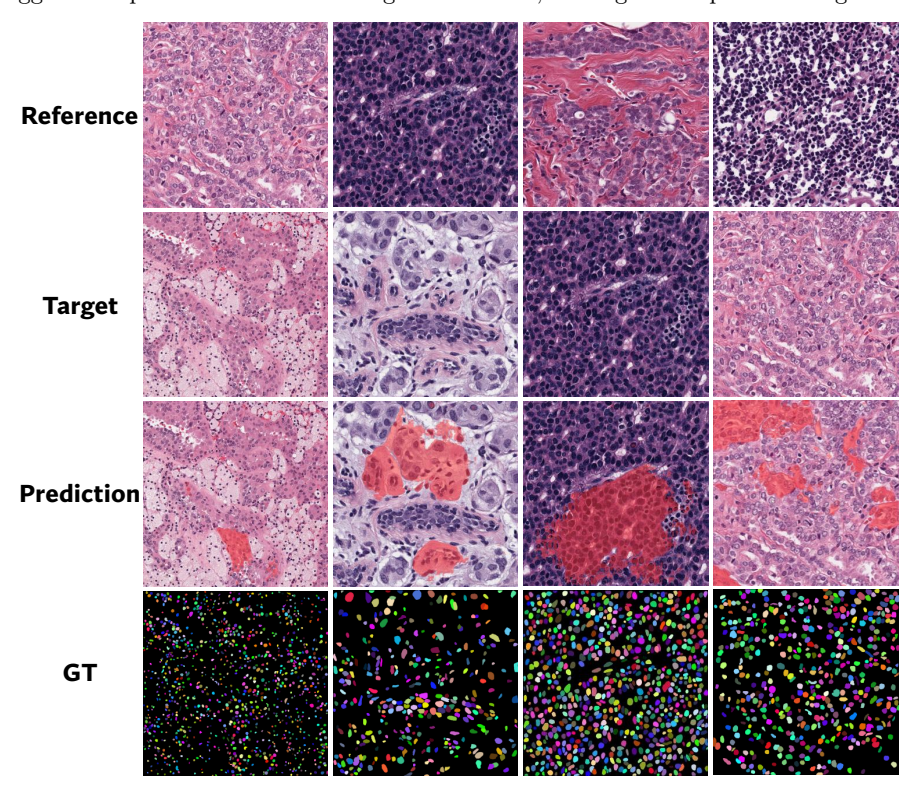


Figure 20 Visualization of semantic segmentation results from Bridge the Points. Red areas represent the segmented regions. Designed for natural images, the method fails to capture scattered nuclei or distinguish individual cells, causing predictions to focus on a few prominent areas and merge many nuclei together.

CutLER (Cut-and-Learn). CutLER is a framework for unsupervised object detection and instance segmentation. It builds on MaskCut, which generates coarse object masks from self-supervised Vision Trans-

former features, and then refines them through detector training with robust loss dropping and iterative self-training. Operating entirely without human annotations, it provides a strong baseline for natural image segmentation.

In our experiments, only the MaskCut stage is applied to produce instance masks, without training the entire network. Because its affinity matrix relies on feature similarity, which is often weakly distinguishable in pathological images, CutLER primarily segments regions with sharp boundary contrasts but is unable to identify small-scale nuclei, as illustrated in Figure 18. Additionally, many nuclear regions remain undetected due to feature homogeneity.

Bridge the Points. Bridge the Points is a graph-based extension of SAM designed for few-shot semantic segmentation. It automatically selects informative prompts and aligns them with mask granularity through graph connectivity, reducing reliance on hyperparameters and redundant mask refinement. This makes it suitable for low-data settings and cross-domain generalization.

In our experiments, semantic masks from reference images were provided together with random target images in a one-shot configuration. As shown in Figure 20, the method improves the delineation of multiple smaller regions compared to other semantic approaches but still operates largely at the tissue level and fails to resolve nuclei at the instance level. Alongside the results from the instance segmentation baselines, this highlights the limitations of directly applying natural image models to the pathological domain.

D Additional Ablation Study

In this section, we report comprehensive segmentation results on MoNuSeg, CPM17, TNBC, and PanNuke across all feature extraction backbones (Section D.2). The complete sets of evaluation metrics, together with additional ablation studies on point generation and post-processing, are provided in Section D.3 and Section D.4, respectively. In Section D.1, we further evaluate the impact of backbone size to assess the practical applicability of SPROUT under limited-resource settings.

D.1 Backbone Variants

To assess the applicability of our method under constrained computational budgets, we evaluated feature extractors of different sizes. Since pathology-specific backbones do not provide multiple capacity tiers, we adopted the ViT family for backbone scaling. The results in Figure 21 indicate that AJI degrades only marginally as the backbone becomes smaller. The large and base variants perform comparably, while the small and tiny variants remain within 2% of the larger models. This mild performance drop can be attributed to the relatively low visual complexity of pathology nuclei, where smaller models still capture sufficiently discriminative features. Moreover, the proposed self-reference strategy in our pipeline provides per-image calibration, further stabilizing the quality of features for point generation. This demonstrates the minimal computational trade-off when reducing

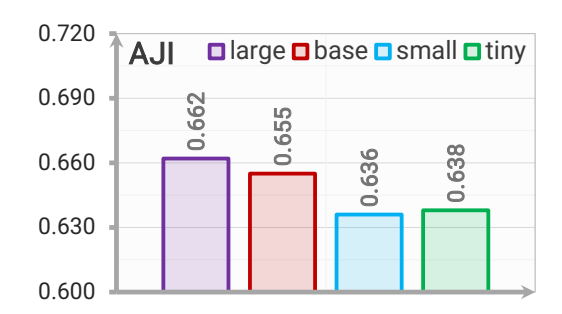


Figure 21 Effects of backbone variants. Results are reported using Vision Transformer backbones on the CPM17 dataset. Feature extraction resolution: 128×128 . SAM weights: large. SAM prediction patch size: 512×512 .

backbone capacity. Overall, these findings suggest that our method remains highly effective even with lightweight backbones, making it well-suited for deployment in resource-limited settings.

D.2 Feature Extractors across Datasets

We present detailed segmentation results on the MoNuSeg, CPM17, TNBC, and PanNuke datasets across different backbones and patch sizes (Table 3–13). The best results are highlighted in **bold**, and the second-best are <u>underlined</u>. These results confirm the effectiveness of our self-reference strategy, showing consistent generalization and comparable performance between natural-image-based and pathology-specific backbones.

Unless otherwise specified, all subsequent predictions are obtained using the large SAM model with a patch size of 512×512 with an overlap ratio of 0.5. Soft NMS is employed as the post-processing method.

Table 3 Segmentation results of AJI and Dice with different backbones on the MoNuSeg dataset.

Backbones	64	128	AJI 256	512	1024	64	128	Dice 256	512	1024
UNI	0.580	0.593	0.606	0.593	0.599	0.772	0.795	0.787	0.766	0.778
UNI2	0.582	0.615	0.602	0.577	0.576	0.774	0.780	0.777	0.760	0.761
Virchow	0.590	0.613	0.621	0.575	0.579	0.764	0.787	0.780	0.759	0.762
Virchow2	0.614	0.622	0.604	0.581	0.575	0.770	0.795	0.776	0.763	0.759
H-optimus-1	0.582	0.599	0.577	0.568	0.573	0.772	0.785	0.781	0.751	0.752
ViT-l/16	0.592	0.606	0.596	0.569	0.570	0.764	0.784	0.768	0.760	0.758
DINOv2	0.598	0.609	0.598	0.582	0.572	0.770	0.784	0.777	0.764	0.756
DINOv3	0.612	0.617	0.612	0.596	0.589	0.779	0.789	0.780	0.766	0.773

Table 4 Segmentation results of DQ and SQ with different backbones on the MoNuSeg dataset.

Daalahaasa			DQ					\overline{SQ}		
Backbones	64	128	256	512	$\boldsymbol{1024}$	64	128	256	$\bf 512$	$\boldsymbol{1024}$
UNI	0.752	0.805	0.793	0.774	0.772	0.730	0.731	0.733	0.729	0.723
UNI2	0.751	0.803	0.792	0.762	0.769	0.732	0.733	0.733	0.730	0.726
Virchow	0.749	0.809	0.792	0.756	0.770	0.733	0.732	0.732	0.729	0.727
Virchow2	0.785	0.817	0.803	0.770	0.762	0.734	0.736	0.733	0.731	0.728
H-optimus-1	0.767	0.796	0.795	0.762	0.763	0.733	0.733	0.735	0.729	0.726
ViT-l/16	0.764	0.797	0.785	0.751	0.762	0.739	0.731	0.731	0.728	0.725
DINOv2	0.764	0.796	0.795	0.767	0.763	0.730	0.731	0.732	0.730	0.726
DINOv3	0.789	0.813	0.817	0.780	0.777	0.731	0.734	0.734	0.729	0.728

Table 5 Segmentation PQ results with different backbones on the MoNuSeg Dataset.

Backbones	64	128	256	512	1024
UNI	0.549	0.588	0.581	0.564	0.558
UNI2	0.550	0.589	0.581	0.556	0.558
Virchow	0.549	0.592	0.580	0.551	0.560
Virchow2	0.576	0.601	0.589	0.563	0.555
H-optimus-1	0.562	0.583	0.584	0.555	0.554
ViT-l/16	0.565	0.582	0.574	0.547	0.552
DINOv2	0.558	0.582	0.582	0.560	0.554
DINOv3	0.577	0.597	0.600	0.569	0.566

Table 6 Segmentation results of AJI and Dice with different backbones on the CPM17 dataset.

De alabassas		A	JI			Dice					
Backbones	64	128	256	512	64	128	256	$\bf 512$			
UNI	0.641	0.651	0.639	0.594	0.805	0.812	0.802	0.769			
UNI2	0.645	0.652	0.642	0.596	0.803	0.815	0.802	0.762			
Virchow	0.643	0.649	0.646	0.599	0.805	0.812	0.807	0.769			
Virchow2	0.642	0.640	0.635	0.592	0.794	0.806	0.787	0.768			
H-optimus-1	0.651	0.662	0.643	0.580	0.804	0.818	0.795	0.765			
ViT-l/16	0.649	0.654	0.642	0.583	0.809	0.810	0.804	0.759			
DINOv2	0.643	0.649	0.637	0.584	0.805	0.809	0.800	0.759			
DINOv3	0.648	0.657	0.637	0.595	0.805	0.821	0.799	0.766			

Table 7 Segmentation results of DQ and SQ with different backbones on the CPM17 dataset.

Backbones		D	$\overline{\mathbf{Q}}$		\mathbf{SQ}				
Dackbones	64	128	256	512	64	128	256	512	
UNI	0.777	0.787	0.787	0.739	0.768	0.770	0.771	0.763	
UNI2	0.771	0.786	0.780	0.739	0.763	0.768	0.770	0.763	
Virchow	0.773	0.781	0.793	0.743	0.769	0.771	0.768	0.764	
Virchow2	0.767	0.780	0.783	0.738	0.768	0.769	0.770	0.768	
H-optimus-1	0.774	0.796	0.776	0.734	0.768	0.774	0.770	0.763	
ViT-l/16	0.784	0.789	0.787	0.725	0.767	0.769	0.772	0.761	
DINOv2	0.783	0.789	0.780	0.726	0.768	0.767	0.771	0.766	
DINOv3	0.788	0.794	0.789	0.747	0.768	0.770	0.772	0.766	

Table 8 Segmentation PQ results with different backbones on the CPM17 Dataset.

Backbones	64	128	256	512
UNI	0.597	0.606	0.606	0.564
UNI2	0.588	0.604	0.601	0.564
Virchow	0.594	0.602	0.609	0.568
Virchow2	0.589	0.600	0.602	0.567
H-optimus-1	0.594	0.616	0.599	0.560
ViT-l/16	0.601	0.607	0.608	0.552
DINOv2	0.601	0.605	0.604	0.556
DINOv3	0.605	0.611	0.609	0.572

Table 9 Segmentation results of AJI and Dice with different backbones on the TNBC dataset.

D 11		A	JI		Dice				
Backbones	64	128	256	$\bf 512$	64	128	256	$\bf 512$	
UNI	0.601	0.600	0.587	0.566	0.767	0.773	0.761	0.746	
UNI2	0.602	0.593	0.587	0.577	0.761	0.765	0.761	0.754	
Virchow	0.595	0.605	0.593	0.568	0.767	0.775	0.766	0.747	
Virchow2	0.592	0.599	0.575	0.565	0.767	0.769	0.752	0.742	
H-optimus-1	0.603	0.600	0.576	0.574	0.768	0.780	0.753	0.748	
ViT-l/16	0.609	0.604	0.594	0.570	0.774	0.766	0.766	0.746	
DINOv2	0.606	0.596	0.581	0.567	0.772	0.766	0.755	0.747	
DINOv3	0.595	0.576	0.580	0.576	0.761	0.759	0.756	0.754	

Table 10 Segmentation results of DQ and SQ with different backbones on the TNBC dataset.

Backbones		D	Q		SQ			
backbones	64	128	256	512	64	128	256	512
UNI	0.783	0.788	0.782	0.766	0.785	0.788	0.787	0.781
UNI2	0.780	0.790	0.787	0.767	0.789	0.787	0.786	0.782
Virchow	0.780	0.796	0.794	0.767	0.785	0.787	0.784	0.781
Virchow2	0.792	0.795	0.776	0.763	0.786	0.785	0.786	0.784
H-optimus-1	0.785	0.794	0.774	0.775	0.787	0.786	0.783	0.779
ViT-l/16	0.794	0.793	0.788	0.768	0.782	0.785	0.785	0.781
DINOv2	0.794	0.796	0.781	0.772	0.784	0.787	0.785	0.778
DINOv3	0.784	0.783	0.771	0.775	0.788	0.785	0.785	0.781

Table 11 Segmentation PQ results with different backbones on the TNBC Dataset.

Backbones	64	128	256	512
UNI	0.615	0.621	0.615	0.598
UNI2	0.615	0.622	0.619	0.600
Virchow	0.612	0.626	0.622	0.599
Virchow2	0.623	0.624	0.610	0.598
H-optimus-1	0.618	0.624	0.606	0.604
ViT-l/16	0.621	0.623	0.619	0.600
DINOv2	0.622	0.626	0.613	0.601
DINOv3	0.618	0.615	0.605	0.605

Table 12 Segmentation results of AJI and Dice with different backbones on the PanNuke dataset.

Backbones	64	AJI 128	256	64	Dice 128	256
UNI	0.571	0.578	0.572	0.757	0.763	0.756
UNI2	0.574	0.580	0.571	0.760	0.766	0.759
Virchow	0.574	0.578	0.575	0.759	0.764	0.762
Virchow2	0.563	0.569	0.562	0.751	0.756	0.752
H-optimus-1	0.576	0.580	0.566	0.761	0.766	0.754
ViT-l/16	0.577	0.581	0.568	0.762	0.766	0.756
DINOv2	0.578	0.577	0.563	0.762	0.763	0.753
DINOv3	0.571	0.571	0.573	0.758	0.758	0.760

Table 13 Segmentation results of DQ, SQ, and PQ with different backbones on the PanNuke dataset.

Da alab assas		DQ			SQ			PQ	
Backbones	64	128	256	64	128	256	64	128	256
UNI	0.685	0.689	0.692	0.760	0.761	0.758	0.521	0.524	0.525
UNI2	0.687	0.699	0.695	0.760	0.762	0.759	0.522	0.533	0.528
Virchow	0.690	0.699	0.696	0.760	0.760	0.759	0.524	0.531	0.528
Virchow2	0.679	0.687	0.696	0.760	0.760	0.760	0.516	0.522	0.529
H-optimus-1	0.687	0.700	0.688	0.761	0.763	0.757	0.523	0.534	0.521
ViT-l/16	0.693	0.700	0.687	0.761	0.760	0.757	0.527	0.532	0.520
DINOv2	0.695	0.697	0.684	0.761	0.761	0.757	0.529	0.530	0.518
DINOv3	0.690	0.694	0.683	0.759	0.760	0.760	0.524	0.527	0.519

Table 14 Comprehensive ablation results of point generation on MoNuSeg. Partial denotes POT-Scan, while balanced refers to standard OT. When OT is not applied, similarity mapping is performed using a greedy strategy. The baseline corresponds to SAM auto-prompting.

Color Prior	Similarity Mapping	OT	AJI	PQ	DQ	\mathbf{SQ}	Dice
Mask	Similarity Mapping	01	AJI	ΓQ	ьф	SQ	Dice
x	Х	Х	0.061	0.262	0.384	0.752	0.353
Otsu	×	×	0.527	0.468	0.634	0.738	0.725
Otsu	\checkmark	×	0.532	0.468	0.636	0.736	0.728
Otsu	\checkmark	balanced	0.545	0.474	0.647	0.732	0.742
Otsu	\checkmark	partial	0.579	0.485	0.661	0.733	0.767
High-confidence	\checkmark	×	0.543	0.479	0.652	0.735	0.738
High-confidence	\checkmark	balanced	0.567	0.510	0.686	0.743	0.759
High-confidence	\checkmark	partial	0.619	0.577	0.787	0.733	0.795

D.3 Point Quality and Generation

We report the detailed quantitative metrics corresponding to the ablation results presented in Section 4.2 Figure 7 in Table 14. These results provide a comprehensive view of how each component contributes to the overall segmentation performance.

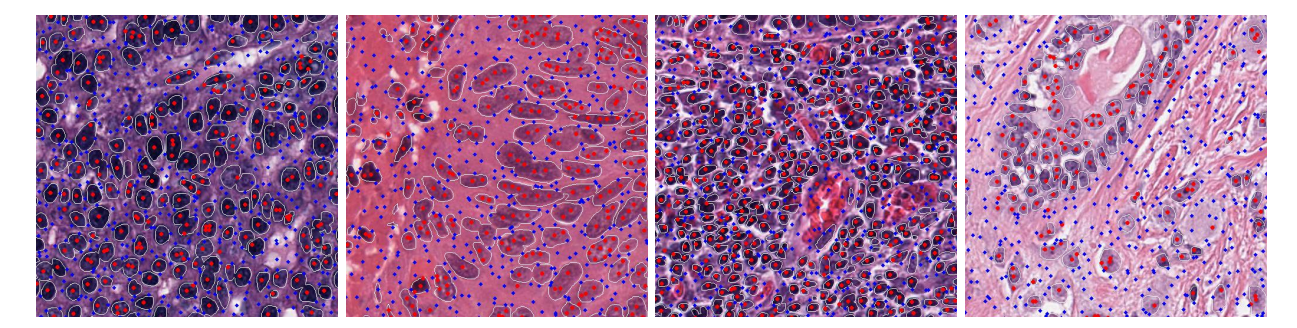


Figure 22 Visualization of point prompts. (MoNuSeg) Positive prompts (red dots) and negative prompts (blue squares) are overlaid on the images to illustrate the quality of prompt selection, with white contours denoting the ground-truth cell boundaries. Images are cropped for clarity of visualization.

Table 15 Evaluation of the generated point prompt quality on different datasets. The prompts exhibit high accuracy, with reliable positive-point coverage and robust background suppression from negative points.

Datasets	\mathbf{TP}	TN	\mathbf{FP}	$\mathbf{F}\mathbf{N}$
MoNuSeg	0.849	0.151	0.943	0.057
CPM17	0.873	0.127	0.956	0.044
TNBC	0.818	0.182	0.982	0.018

To evaluate the generated point prompts both quantitatively and qualitatively, we present the visualization of the point spatial distribution overlaid with the images in Figure 22 and the direct accuracy of both positive and negative points across the three datasets in Table 15. Overall, both positive and negative prompts exhibit high precision, with negative points achieving particularly strong true positive rates by effectively avoiding non-cell areas. Positive points also demonstrate robust coverage since they reliably capture nuclei even in densely packed regions with small cells. For larger nuclei, multiple positive points are often assigned within a single object, further increasing the possibility of accurate segmentation. Only a minor fraction of very small or weakly stained nuclei may be underrepresented, reflecting inherent challenges in such pathological settings. This strong alignment supports the downstream instance prediction, as accurate point allocation provides a reliable foundation for mask generation.

D.4 Soft NMS

In this section, we present a comprehensive evaluation of the proposed post-processing strategy. We report detailed performance metrics and ablation studies on the score and decay functions of soft NMS to validate the method. We further include visualizations and pseudo-code to illustrate the procedure.

Table 16 Detailed ablation results of post-processing strategy on MoNuSeg. CP denotes containment penalty.

CP	NMS	AJI	PQ	DQ	\mathbf{SQ}	Dice
X	hard	0.553	0.523	0.712	0.735	0.743
X	soft	0.573	0.529	0.726	0.729	0.765
X	hard+soft	0.565	0.534	0.719	0.743	0.757
\checkmark	hard	0.585	0.573	0.785	0.730	0.764
\checkmark	soft	0.620	0.593	0.809	0.733	0.789
\checkmark	hard+soft	0.605	0.576	0.788	0.731	0.778

Table 17 Ablation of score strategies for soft NMS on MoNuSeg. Results highlight different focuses between H-channel response and SAM confidence. The combined approach provides the most balanced improvement in post-processing.

Strategy	AJI	PQ	DQ	\mathbf{SQ}	Dice
×	0.546	0.364	0.495	0.735	0.747
S_H'	0.591	0.581	0.793	0.733	0.784
S_{SAM}	0.587	0.583	0.792	0.732	0.781
$S_H' + S_{SAM}$	0.619	0.593	0.809	0.734	0.792

Table 18 Ablation of decay functions for soft NMS on MoNuSeg. All soft NMS variants outperform hard NMS. Exponential decay achieves the best overall performance by more effectively penalizing heavily overlapping instances while preserving valid detections.

Functions	AJI	\mathbf{PQ}	$\mathbf{D}\mathbf{Q}$	\mathbf{SQ}	Dice
hard	0.587	0.549	0.761	0.721	0.764
linear	0.601	0.564	0.774	0.729	0.778
polynomial	0.599	0.568	0.778	0.731	0.780
exponential	0.614	0.577	0.787	0.733	0.787

As a complement to Figure 7b, Table 16 reports the detailed ablation results of the NMS strategy across all five evaluation metrics.

To assess the necessity of the combined score strategy, we compare H-channel response alone, SAM confidence score alone, and their combination, with the raw predictions as the baseline. As shown in Table 17, applying soft NMS improves the overall segmentation performance compared with directly aggregating predictions. Both the H-channel response and the SAM score alone further enhance performance. This highlights the importance of incorporating image-derived cues when refining instance predictions. The H-channel emphasizes heavily stained regions but tends to keep darker tissue areas. In contrast, the SAM score favors nuclei with clear boundaries, preserving large nuclear regions but failing to separate overlapping cells. The combined strategy effectively balances these complementary strengths and achieves the best overall performance.

We further investigate the effect of different score decay functions in soft NMS, including linear, polynomial, and Hard NMS, as a conexponential. ventional suppression scheme, is employed as the baseline. marized in Table 18, all variants of Soft-NMS consistently outperform hard NMS across multiple metrics, underscoring the advantage of retaining slight overlapping predictions with gradually decayed scores rather than discarding them. This flexible suppression handles dense cell regions better. Among the tested functions, the exponential decay yields the best overall performance. This can be attributed to the fact that exponential decay provides a sharper penalty to highly overlapping instances

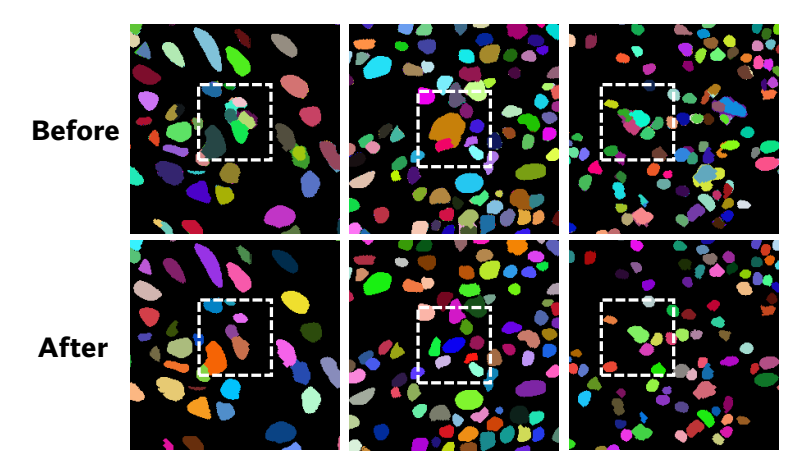


Figure 23 Visualization of soft NMS post-processing. The containment-aware variant effectively suppresses large predicted masks that contain smaller ones, leading to cleaner and more precise outputs. The highlighted regions show distinct differences.

while still preserving moderately overlapping candidates. It strikes a better balance between suppressing redundant detections and retaining true positives in the post-processing procedure. The effectiveness of soft NMS with the exponential decay function is illustrated in Figure 23.

Lastly, we provide the comprehensive pseudo-code of the containment-aware soft NMS in Alg.(3).

E Additional Sensitivity Analysis

E.1 SAM Effect.

SAM is highly sensitive to the form of inputs. Naïve application often leads to suboptimal performance on pathology images due to densely packed structures, heterogeneous staining, and subtle nuclear boundaries. The strategies illustrated in the Figure 24 are designed to mitigate these challenges.

Image size. As illustrated in Figure 24a, scaling controls the receptive field over which SAM attends. Without scaling, SAM can respond to large tissue regions, ignoring fine-grained nuclear detail. By splitting the image into small patches, the model is guided to treat individual nuclei as primary segmentation targets.

Negative prompts. In histology images, nuclei are frequently embedded within complex backgrounds where clear boundaries are lacking. As shown in Figure 24b, negative prompts act as explicit counterexamples, guiding SAM to disregard surrounding tissue that mimics nuclear appearance. This strategy mitigates over-segmentation and enhances boundary precision.

Positive prompt placement. Overlapping or touching nuclei pose a significant challenge, as SAM may merge them into a single mask in Figure 24c. Carefully placing positive prompts within each nucleus provides local anchors that enforce instance-level separation, enabling SAM to segment individual objects rather than clusters.

Together, these strategies systematically adapt SAM's general-purpose design to the demands of nuclear segmentation. They highlight that effective use of SAM in computational pathology depends not only on model capacity but also on thoughtful construction of inputs that reflect domain-specific image structure.

Algorithm 3 Containment-aware Soft NMS

```
1: Inputs: Masks \{M_i\}_{1}^{n}, scores \{S_i\}_{1}^{n}
 2: Exponential decay f(x) = \exp(-x^2/\sigma) with \sigma > 0,
      penalty scale \epsilon > 0, score threshold \tau.
 3:
 4: \mathcal{B} \leftarrow \emptyset
 5: \mathcal{D} \leftarrow \{(M_i, S_i)\}_{i=1}^n
                                                ▶ working set of detections
 7: for each (M_i, S_i) \in \mathcal{D} do
            if N_{\text{contained}}(M_i) > 1 then
                   S_i \leftarrow S_i \cdot (1 - \tanh(\epsilon \cdot N_{\text{contained}}(M_i)))
 9:
             end if
10:
11: end for
13: while \mathcal{D} \neq \emptyset do
             (M_{\max}, S_{\max}) \leftarrow \arg \max_{(M,S) \in \mathcal{D}} S
14:
            \mathcal{B} \leftarrow \mathcal{B} \cup \{M_{\text{max}}\}
15:
16:
            \mathcal{D} \leftarrow \mathcal{D} \setminus \{(M_{\text{max}}, S_{\text{max}})\}
             for each (M_i, S_i) \in \mathcal{D} do
17:
                   b_{\text{max}} \leftarrow \text{bbox}(M_{\text{max}}), \quad b_i \leftarrow \text{bbox}(M_i)
18:
                   u \leftarrow \text{IoU}(b_{\text{max}}, b_i)
19:
                   S_i \leftarrow S_i \cdot f(u)
20:
                   if S_i < \tau then
21:
                        \mathcal{D} \leftarrow \mathcal{D} \setminus \{(M_i, S_i)\}
22:
                   end if
23:
24:
            end for
25: end while
26:
27: return \mathcal{B}
```

F Discussion and Future Directions

F.1 Beyond H&E

SPROUT is fundamentally designed for H&E pathology images, where the stain-derived optical density provides a biochemical prior for constructing high-confidence foreground and background masks to guide prototype formation. Consequently, all main experiments in the paper focus on H&E nuclear segmentation.

To explore the extensibility of the proposed framework, we conducted a qualitative experiment on fluorescent nuclei images from the DSB2018 dataset (Caicedo et al., 2019). For this modality, we replace the stain-prior module with a fluorescence-intensity prior, where bright emission regions correspond to nuclear structures. Since no backbone is specifically trained for fluorescent microscopy images, we adopt natural-image pretrained backbones instead to extract features for prototype construction and POT-scan refinement.

Despite the absence of color semantics, SPROUT's prototype clustering and POT-scan refinement remain effective. As shown in Figure 25, the resulting segmentation closely matches the provided ground truth.

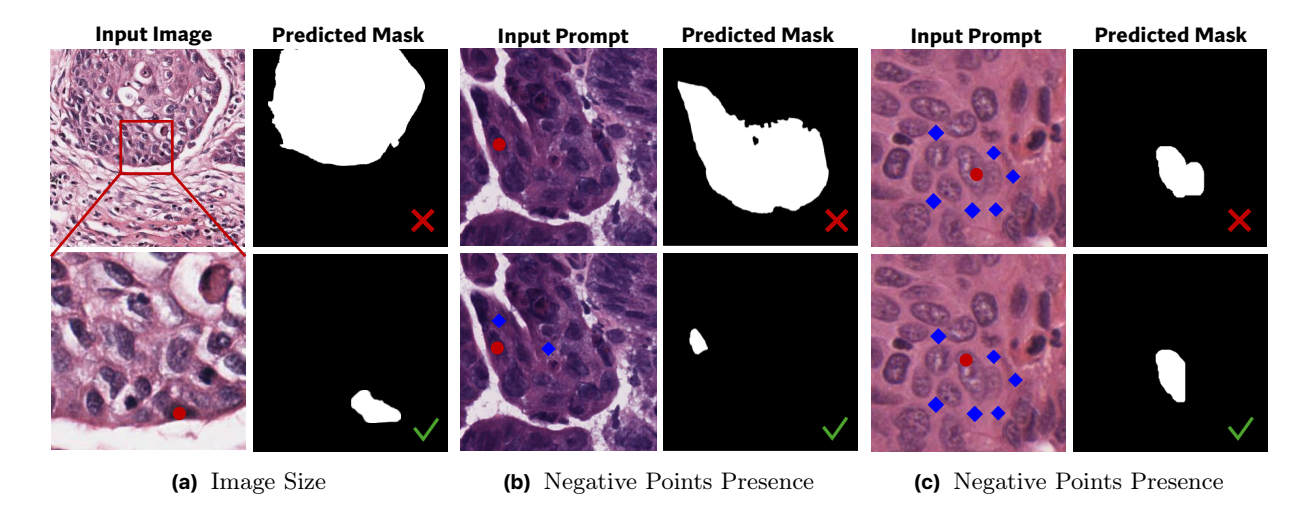


Figure 24 Illustration of SAM effect. (a) Appropriate image cropping enables SAM to focus on local nuclei instead of broad tissue regions. (b) Incorporating negative prompts suppresses background responses for precise nuclear delineation, which is especially valuable in images where stained tissue and nuclei exhibit similar colors. (c) The placement of positive prompts influences the separation of overlapping nuclei. Red dots denote positive prompts and blue squares denote negative prompts.

These results suggest that the core mechanism of SPROUT is not bound to H&E-specific color cues, but can operate as long as the modality provides reliable signals to distinguish foreground nuclei from background tissue.

This observation highlights a promising direction for future work. SPROUT can potentially be extended to other imaging modalities by developing modality-specific cues, such as color characteristics, intensity patterns, or structural contrast, to generate high-confidence foreground and background indicators for self-reference and feature allocation. We hope that SPROUT will motivate further exploration on training-free strategies for nuclear segmentation and encourage the community to investigate a broader range of cellular imaging modalities beyond traditional H&E pathology.

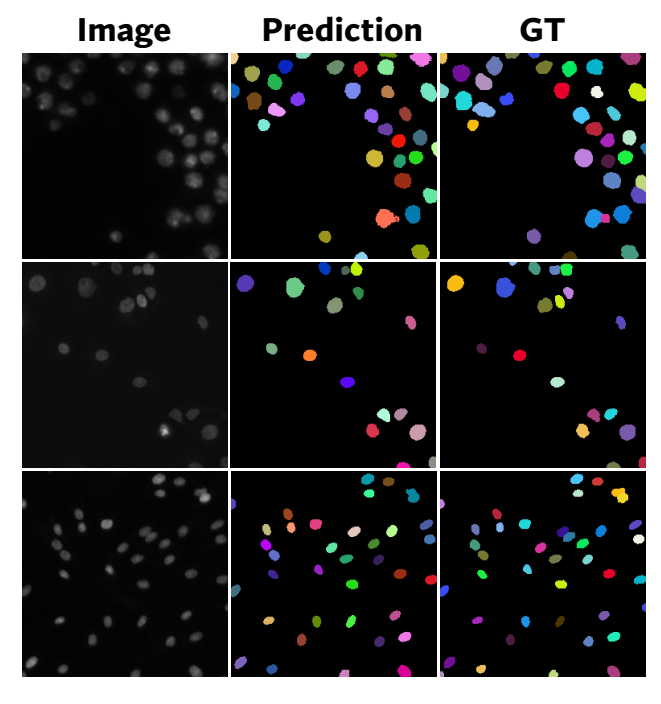


Figure 25 Visualization of fluorescent nuclei segmentation on the DSB2018 dataset. SPROUT is implemented with a ViT backbone for feature extraction, and SAM-Large for instance prediction.